Joint Resource Management for Intelligent Reflecting Surface–Aided Visible Light Communications

Shiyuan Sun, Fang Yang, *Senior Member, IEEE*, Jian Song, *Fellow, IEEE*, and Zhu Han, *Fellow, IEEE*

***Abstract*— Though visible light communication (VLC) is a significant supplement to current communication technologies, disadvantages such as the sensitivity to obstacles limit its development and commercialization. As a revolutionizing technology, intelligent reflecting surface (IRS) offers an ability to reconfigure the wireless environment dynamically and passively, which is considered beneficial to improve the performance of VLC. This paper devotes to investigating the effect of VLC IRS and putting forward a joint resource management method for an instantaneous IRS-aided VLC system. To this end, the line-of-sight (LoS) and non-LoS channel gains are first discussed under the point source assumption, after which the system model is established and the optimization problem is formulated. Then, the frozen variable algorithm and minorization-maximization algorithm are proposed to iteratively maximize the overall spectral efficiency (SE), and detailed discussions on the weak/severe interference cases and computational complexity analysis are carried out. Moreover, numerical results are provided to show the improvement of SE and the effects of the proposed algorithms, which offers beneficial insights on joint resource management of IRS-aided VLC.**

***Index Terms*— Visible light communication (VLC), intelligent reflecting surface (IRS), spectral efficiency maximization, joint resource management, frozen variable algorithm, minorization-maximization algorithm.**

I. Introduction

RECENTLY, the academic research and commercial deployment of the fifth-generation (5G) and beyond communications are in full swing, including sub-6G and millimeter-wave communication technologies. Nevertheless, the traffic volume of the wireless networks will grow up by thousands-fold in the foreseeable future, which imposes a lot for the crowded and fragmented frequency resources in the radio frequency (RF) range [1]. To meet the requirements of forthcoming wireless communications, visible light communication (VLC) shows unique advantages, including the broad bandwidth, high physical layer security, no interferences with RF communications, and the ubiquity of light-emitting diodes (LEDs) [2]. Abundant foundational research has been investigated around the channel gain derivation [3] and channel capacity analysis [4]–[6], and also VLC multiple-input and multiple-output techniques [7] and dimming control approaches [8] are two important branches of VLC. In the meantime, the progress of VLC industrialization has attracted much attention, and a growing number of international organizations have been established to promote its commercialization, including Visible Light Communication Consortium (VLCC) from Japan, OMEGA-the Home Gigabit Access Project from the European Union, and WPAN Visual Light Communication Interest Group (IGvlc) from the society of IEEE [1], [2]. Even so, the VLC technology still remains extensive pending problems, among which the propagation distance is limited due to the unique properties of the visible light. Moreover, it is generally believed that VLC cannot penetrate obstacles due to the high penetration loss [9], and the illumination requirements pose a challenge to the practicality of VLC.

Intelligent reflecting surface (IRS) is an emerging technology that exploits the non-line-of-sight (NLoS) paths to enhance the capability of wireless communication systems. The principle of IRS lies in the manipulations of induction current patterns after the electromagnetic wave impinges the surface, which is a two-dimensional planar periodically made of artificial atoms. Related studies in the RF range include the joint passive and active beamforming design [10], the deep reinforcement learning-based IRS [11], channel estimation for IRS [12], etc. However, due to the nonnegative and real-valued amplitude and other differences, these technologies cannot be directly extended into VLC, and the research on IRS-aided VLC is just beginning. In the mainstream, there are two feasible hardware architectures of IRS in the visible light range, namely the mirror array-based IRS [13], [14] and the metasurface-based IRS [15]. The former implementation is based on geometric optics like Snell's law of reflection, and

Manuscript received 27 August 2021; revised 17 December 2021; accepted 3 February 2022. Date of publication 16 February 2022; date of current version 12 August 2022. This work was supported in part by the National Natural Science Foundation of China under Grant 61871255, in part by the Beijing National Research Center for Information Science and Technology under Grant BNR2022RC01017, in part by the Fok Ying Tung Education Foundation, and in part by NSF under Grant CNS-2107216 and Grant EARS-1839818. The associate editor coordinating the review of this article and approving it for publication was L. Dasilva. *(Corresponding author: Fang Yang.)*

Shiyuan Sun, Fang Yang, and Jian Song are with the Department of Electronic Engineering, Beijing National Research Center for Information Science and Technology, Tsinghua University, Beijing 100084, China, and also with the Key Laboratory of Digital TV System of Guangdong Province and Shenzhen City, Research Institute of Tsinghua University in Shenzhen, Shenzhen 518057, China (e-mail: sunsy20@mails.tsinghua.edu.cn; fangyang@tsinghua.edu.cn; jsong@tsinghua.edu.cn).

Zhu Han is with the Department of Electrical and Computer Engineering, University of Houston, Houston, TX 77004 USA, and also with the Department of Computer Science and Engineering, Kyung Hee University, Seoul 446-701, South Korea (e-mail: zhan2@uh.edu).

Color versions of one or more figures in this article are available at https://doi.org/10.1109/TWC.2022.3150021.

Digital Object Identifier 10.1109/TWC.2022.3150021

each unit can rotate around two independent and orthogonal axes similar to micro-electro-mechanical systems [13], [14]. Then, the second hardware exploits dielectric structures or sub-wavelength metallic to abnormally manipulate the propagation behavior, and the structures in the near-infrared range (NIR) and visible light range are developed in [16], [17], respectively. On the other hand, follow-up works focus on the channel gain analyses of the NLoS links reflected by IRS [13]–[15], and in particular, an upper bound of the irradiance intensity level is given in [15] under the point source condition, which follows an "additive" model due to the near field assumption [18]. Also, the reflection behavior is investigated in the free space optical system, and it reveals that the outage probability can be reduced by IRS [19], [20]. Based on the above foundation studies, the authors in [21] categorize the advantages of IRS-aided VLC into three main aspects, namely the signal coverage expansion, the illumination requirement relaxation, and the signal power enhancement. Then, the IRS configuration policy is optimized for the sum rate maximization, and numerical results indicate that IRS can address blockage problems to an extent [22], [23]. Moreover, the research shows that the physical layer security of VLC systems can also be improved by IRS [24].

Under the point source assumption, this paper endeavors to jointly optimize the IRS configuration, the power allocation, and the user association behavior in an individual time slot of the time division multiple access (TDMA) VLC system. To this end, the channel models of the line-of-sight (LoS) link and NLoS link are elaborated, and the instantaneous signal expression is derived as the objective of the spectral efficiency (SE) maximization problem. Specifically, the contributions of the paper are summarized as follows:

- One highlight is defining a binary IRS coefficient matrix, by which the configuration process is abstract into a binary programming problem and complicated triangular transformations and geometric operations are avoided. After this matrix is optimized, the physics coefficients of each unit can be obtained by reverse lookup tables, which are generated in advance by mapping the angles of reflected light to unit coefficients. This method is feasible since the indoor VLC channel gain sensitively depends on the geometric locations of transceivers and IRS units, which are assumed known to the system controller.
- This paper proposes an alternating optimization algorithm to maximize the overall SE of the IRS-aided multi-user VLC system. Particularly, the variable frozen algorithm is proposed to solve the IRS configuration subproblem in reduced complexity, and the numbers of variables and constraints decrease in the scale of $\min(1, K/L)$, where K and L denote the numbers of users and transmitters, respectively. Moreover, the minorization-maximization (MM) algorithm is utilized to solve the power allocation subproblem and user association subproblem, which are non-convex problems and conventional convex optimization tools cannot be used directly.
- Theoretical analyses on extremely weak/severe interferences cases and the computational complexity of the proposed algorithms are carried out in the paper. Then, extensive numerical results are executed to verify the SE improvement of the proposed algorithms over other baselines, and it is also observed that the SE gain from IRS is almost linear to the number of IRS units and the reflection factor. Moreover, considering IRS configuration depends highly on geometric factors, the analysis of the locations and IRS size is provided detailly.

TABLE I
SYMBOL NOTATIONS

Symbol	Description
K	The number of users (PDs)
L	The number of transmitters (LEDs)
N	The number of IRS units
$\mathbf{H}^{(1)}$	The LoS channel gain
$\mathbf{H}^{(2)}$	The NLoS channel gain
C	The channel capacity of VLC
R	The spectral efficiency
$\mathbf{G}$	The IRS coefficient matrix
$\mathbf{P}$	The power allocation matrix
$\mathbf{F}$	The user association matrix
$P_{\min}$	The minimum optical power of LED
$P_{\max}$	The maximum optical power of LED
P_{total}	The total maximum optical power

The remainder of the paper is organized as follows: in Section II, the channel gain and signal model are discussed elaborately. Then, the optimization problem is formulated in Section III, and an alternating optimization algorithm is proposed by dividing the original problem into three subproblems and solving them iteratively. Afterwards, detailed numerical simulations are carried out in Section IV. Finally, Section V concludes the whole paper.

Notations: normal letters a (or A), boldface letters $\mathbf{a}$, boldface uppercase letters $\mathbf{A}$ represent the scaler values, vectors, and matrices, respectively. Particularly, $\mathbf{I}_N$ denotes an $N \times N$ identity matrix, and diag($\mathbf{a}$) is a diagonal matrix with the elements of $\mathbf{a}$ on the main diagonal. Then, $\mathrm{rank}(\cdot)$, $\mathrm{rank}^{(c)}(\cdot)$, vec$(\cdot)$, $\|\cdot\|_F$, are the symbols of rank, column rank, vectorization operator, Frobenius norm, respectively. Given defined variables, $\oplus$, $\odot$, $|\cdot|$, $(\cdot)^T$, ∂, denote the direct sum operator, Hadamard product, absolute value, transpose, and partial operator, respectively. Moreover, $\mathbb{R}_+$ is defined as the real and positive number set, and calligraphic letter $\mathcal{A}$ denotes the other defined set. The operator supp($\mathbf{a}$) represents the support set of the vector $\mathbf{a}$, and $\mathbf{A}\{\cdot\}$ is a submatrix composed of columns with indices from the inside set.

II. SYSTEM MODEL OF THE IRS-AIDED VLC

Considering the downlink side of an IRS-aided TDMA VLC system, where K users are served by L LEDs and an IRS with N units is equipped to enhance the communications. It is assumed that each LED serves a single user in one time slot, and multi-user interferences (MUI) will be caused among different lamps. Without loss of generality, the user locations and VLC channel state information (CSI) are known

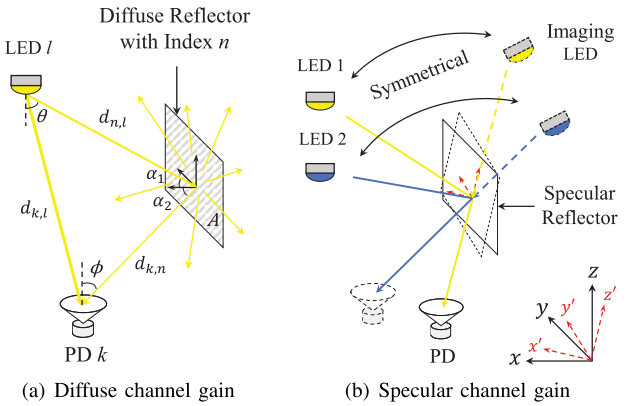

(a) Diffuse channel gain (b) Specular channel gain

Fig. 1. Channel gain of the NLoS path.

at the system controller, which can be accomplished by VLC positioning technologies [25] and various channel estimation methods [26], respectively.

A. Channel Gain of LoS Paths

Suppose the k-th user is served by the l-th LED, its LoS direct gain in VLC generally follows the Lambertian model, which in mathematics is given by [3], [27]

$$h_{k,l}^{(1)} = \frac{(m+1)A}{2\pi d_{k,l}^2} \cos^m(\theta) g_{of} \cos(\phi) f(\phi), \tag{1}$$

where $m = -1/\log_2(\cos(\Theta_{1/2}))$ is the Lambertian index with $\Theta_{1/2}$ the semi-angle at half illuminance of the LED, A is the physical area of the photodetector (PD), $d_{k,l}$ is the distance between the transceivers, and θ and ϕ are the angles of irradiance and incidence, respectively. Then, g_{of} is the optical filter gain, and the optical concentrator gain $f(\phi)$ with respect to field-of-view (FoV) Φ is given in [28]. For simplicity, a generated matrix $\mathbf{H}^{(1)} = [\mathbf{h}_1^{(1)}, \mathbf{h}_2^{(1)}, \ldots, \mathbf{h}_K^{(1)}]^T$ is defined to represent the LoS channel gain, where each column $\mathbf{h}_k^{(1)} = [h_{k,1}^{(1)}, h_{k,2}^{(1)}, \ldots, h_{k,L}^{(1)}]^T$ denotes the direct gain vector between LEDs and the k-th user.

B. Channel Gain of NLoS Paths

In general, NLoS paths in wireless communications include reflection paths, diffraction paths, scattering paths, and penetration paths. Considering the extremely high penetration loss of visible light, the penetration paths are commonly ignored in VLC [9]. Then, the diffraction path is also negligible due to the nanoscale of wavelength. According to the surface properties of the reflector, the light reflection can be categorized into two types: diffusely reflected link and specularly reflected link. The channel gain of these two paths will be investigated and compared in the sequel of this subsection.

1) Diffuse Reflection Path: When the surface is made of an inhomogenous medium, the incident light will be reflected and spread in all directions, which is known as diffuse reflection. As shown in Fig. 1(a), the energy of the reflected light is scattered on the surface of the reflector, and only the part that in a specific direction can be received by the target PD. Based on [29], the channel gain of the first reflected link by the unit area of the reflector can be expressed as

$$h_{k,n,l}^{(\text{Diffuse})} = \frac{\tau(m+1)A}{2\pi d_{n,l}^2 d_{k,n}^2} \cos^m(\theta) \cos(\alpha_1) \cos(\alpha_2) \times g_{of} \cos(\phi) f(\phi), \tag{2}$$

where τ is the reflection factor of the diffuse reflector, $d_{n,l}$ is the distance between the l-th LED and the n-th IRS unit, and $d_{k,n}$ is the distance between the n-th IRS unit and the k-th user. Then, α_1 and α_2 are the angles of irradiance and incidence based on the reflection plane, respectively. Notably, Eq. (2) follows a "multiplicative" model, which is structurally identical to the far field channel gain in RF IRS systems [30].

2) Specular Reflection Path: Specular reflection refers to the situation that the energy loss mainly occurs in the medium absorption, and the reflected light will travel in a unique direction. The surface of the reflector in Fig. 1(b) should be homogenous, including the planar mirror or the medium with compact periodic microstructure. Geometrically, the angle of irradiance equals the angle of incidence, which is also known as Snell's law of reflection [13]–[15]. An upper bound of the irradiance level is derived in [15] under the point source condition as

$$E_{k,n,l}^{(\text{Specular})} = \frac{\delta(m+1)p\cos^m(\theta)}{2\pi(d_{n,l}+d_{k,n})^2} \cos(\phi), \tag{3}$$

where δ and p are the reflection factor and the emission power, respectively. Eq. (3) demonstrates that the specular reflection path can equivalently be regarded as an extended path, consisting of the LED-to-IRS link and IRS-to-PD link. On the other hand, considering the nanoscale wavelength in VLC, the signal propagation distance is smaller than the threshold as

$$L_0 = \frac{2D^2}{\lambda}, \tag{4}$$

where D and λ represent the largest IRS dimension and the wavelength, respectively [18]. Then, the near field assumption is ensured in IRS-aided VLC, and therefore the path loss follows an "additive" model as derived in (3).

To be clear, both diffuse and specular reflection paths coexist in VLC. Nevertheless, the fact has been justified that the path loss by the second diffuse reflections is nearly 25 dB larger than that of LoS path, and even the gain of the one-hop diffuse reflection path is 15 dB lower than the LoS one [9], [28]. As a result, the specular reflection is generally considered as the significant NLoS component in IRS-aided VLC, while diffuse reflection is ignored [13], [15], [19], [24]. Based on (3), the NLoS channel gain can be rewritten as

$$h_{k,n,l}^{(2)} = \delta \frac{(m+1)A}{2\pi(d_{n,l}+d_{k,n})^2} \cos^m(\theta) g_{of} \cos(\phi) f(\phi). \tag{5}$$

Moreover, a matrix $\mathbf{H}^{(2)}$ is defined to denote the NLoS channel gain for simplicity. This matrix is three-dimensional and consists of slices as $\mathbf{H}_k^{(2)} = \text{diag}(\mathbf{h}_{k,1}^{(2)T}, \mathbf{h}_{k,2}^{(2)T}, \ldots, \mathbf{h}_{k,L}^{(2)T}) \in \mathbb{R}_+^{L \times NL}$, where each column $\mathbf{h}_{k,l}^{(2)} = [h_{k,1,l}^{(2)}, h_{k,2,l}^{(2)}, \ldots, h_{k,N,l}^{(2)}]^T$ denotes the NLoS direct gain vector between the l-th LED and the k-th user.

C. Instantaneous Received Signal of IRS-Aided VLC

This subsection devotes to calculating the instantaneous received signal in one time slot. To this end, a user association matrix $\mathbf{F}$ and a power allocation matrix $\mathbf{P}$ are defined to describe the behavior of transmitters, and then a discrete matrix $\mathbf{G}$ is introduced to denote the IRS configuration process. These three matrices are variables to be jointly optimized later, and their descriptions are given in detail as follows.

1) User Association: In a time slot of the TDMA system, let L transmitters carry information symbols of K users, which are denoted by the vector $\mathbf{y} = [y_1, y_2, \ldots, y_K]^T$. Then, suppose the emission signal on LEDs is defined as $\mathbf{x} = [x_1, x_2, \ldots, x_L]^T$, a description of the association behavior between the transceivers is given by

$$\mathbf{x} = \mathbf{F}\mathbf{y}, \tag{6}$$

where $\mathbf{F} = [\mathbf{f}_1, \mathbf{f}_2, \ldots, \mathbf{f}_K]$ is a binary matrix with each column $\mathbf{f}_k \in \mathbb{R}_+^{L\times 1}$ indicating the projections of the information symbol y_k on all transmitters. More specifically, $f_{l,k} = 1$ and 0 represent that the k-th user does or does not accept the l-th LED's service, respectively.

2) Emission Power: As a wireless communication technology that takes into account both communication and illumination functions, both peak and total power constraints cannot be ignored in VLC, and it has been demonstrated that VLC performance gain can be achieved by properly allocating the emission power among different transmitters [28]. In this paper, a diagonal power matrix $\mathbf{P} = \text{diag}\,(P_1, P_2, \ldots P_L)$ is defined to indicate the emission power on LEDs, and therefore the transmit signal can be expressed as $\widetilde{\mathbf{x}} = \mathbf{P}\mathbf{x}$. Based on (6), the LoS received signal of the k-th user is formulated as

$$\hat{y}_k^{(1)} = \rho_k \mathbf{h}_k^{(1)T}\widetilde{\mathbf{x}} = \rho_k \mathbf{h}_k^{(1)T}\mathbf{P}\mathbf{f}_k y_k + \rho_k \sum_{i=1, i\neq k}^{K} \mathbf{h}_k^{(1)T}\mathbf{P}\mathbf{f}_i y_i, \tag{7}$$

where the two components denote the useful signal and the MUIs, respectively.

3) IRS Configuration: Thirdly, an IRS coefficient matrix $\mathbf{G}$ is defined to indicate the relationship between IRS units and transmitters. Specifically, $\mathbf{G} = [\mathbf{g}_1, \mathbf{g}_2, \ldots, \mathbf{g}_L]$ is a binary matrix with column $\mathbf{g}_l \in \mathbb{R}_+^{N\times 1}$ representing the indices of the assigned units for the l-th transmitter, i.e., $g_{n,l} = 1$ means the n-th IRS unit belongs to the l-th LED. Considering the channel model in indoor VLC is determined mainly by the locations of the transceivers, any movement of the transmitter/receiver/reflector may significantly change the channel gain, resulting in the high spatial resolution of the VLC channel. As shown in Fig. 1(b), the specular reflection path can be considered as an extended path emitted from the imaging LED. When an IRS unit is configured well so that the PD can receive the light from LED 1, the reflection path of the LED 2 points at a completely different direction according to Snell's law of reflection. The probability that any other PD happens exactly to be here is (a.s.) 0 in mathematics, which demonstrates that the interferences caused by specular reflection paths are negligible. Therefore, a single IRS unit cannot serve more than one PDs simultaneously, and the NLoS received signal of the k-th user can be expressed as

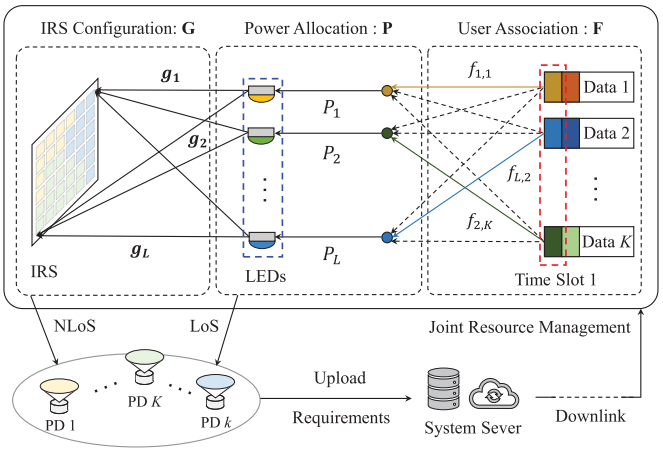

Fig. 2. IRS-aided VLC system model that denotes the process of joint resource management.

$$\hat{y}_{k,l}^{(2)} = \rho_k \sum_{n=1}^{N} h_{k,n,l}^{(2)} g_{n,l} P_l x_l f_{l,k} = \rho_k \mathbf{h}_{k,l}^{(2)T} \mathbf{g}_l P_l x_l f_{l,k}. \tag{8}$$

Then the overall NLoS signal $\hat{y}_k^{(2)} = \sum_{l=1}^{L} \hat{y}_{k,l}^{(2)}$ is given by

$$\begin{aligned}\hat{y}_k^{(2)} &= \rho_k \left[\mathbf{h}_{k,1}^{(2)T}\mathbf{g}_1 P_1 x_1, \ldots, \mathbf{h}_{k,L}^{(2)T}\mathbf{g}_L P_L x_L\right]\mathbf{f}_k \\ &= \rho_k \left[\mathbf{h}_{k,1}^{(2)T}\mathbf{g}_1, \ldots, \mathbf{h}_{k,L}^{(2)T}\mathbf{g}_L\right]\mathbf{P}\text{diag}(\mathbf{x})\mathbf{f}_k \\ &= \rho_k \left[\mathbf{H}_k^{(2)}\text{vec}(\mathbf{G})\right]^T \mathbf{P}\text{diag}(\mathbf{F}\mathbf{y})\mathbf{f}_k. \end{aligned} \tag{9}$$

Notably, the equation $\text{diag}\,(\mathbf{F}\mathbf{y})\,\mathbf{f}_k = y_k\mathbf{f}_k$ holds due to the orthogonality among $\mathbf{f}_k$, and the above formula can be further rewritten by replacing the last two multiplicators as

$$\hat{y}_k^{(2)} = \rho_k \left[\mathbf{H}_k^{(2)}\text{vec}(\mathbf{G})\right]^T \mathbf{P}\mathbf{f}_k y_k. \tag{10}$$

To sum up, the received signal of the k-th user is comprised of the LoS component $\hat{y}_k^{(1)}$, the NLoS component $\hat{y}_k^{(2)}$, and the noise w_k at the receiver modeled by additive Gaussian white noise (AWGN) [28]. The overall received signal $\hat{y}_k$ can be expressed as

$$\hat{y}_k = \hat{y}_k^{(1)} + \hat{y}_k^{(2)} + w_k. \tag{11}$$

A sketch map is provided in Fig. 2 to denote the system model. Specifically, the communication or illumination requirements of users are uploaded to the system controller, which then jointly realizes the downlink resource management by associating the relationship between LEDs and data streams, allocating emission power on each LED, and configuring IRS coefficients by reverse lookup tables. The evaluation indicator of the resource management is the overall SE, and the proposed optimization algorithms and theoretical analyses are provided in the next section.

III. Joint Resource Management for Spectral Efficiency Maximization

Motivated by the aforementioned discussions, this section formulates a combinatorial optimization problem, and an alternating optimization algorithm is proposed to manage system resources jointly. Specifically, the frozen variable algorithm and the MM algorithm are utilized to solve the IRS configuration subproblem and the power allocation/user association subproblems, respectively. Moreover, the discussions on the optimization problems under extremely weak/severe interferences and the computational complexity analysis are also carried out in this section.

A. Problem Formulation

The classic Shannon capacity formula cannot be utilized to describe VLC channel capacity due to several unique constraints, including the nonnegative and real-valued signal, the illumination requirements, and the sensitivity to geometric locations [28]. As a result, the VLC channel capacity has been broadly investigated, and the achieved results reveal that the optimal capacity-input distribution is discrete in VLC [4], [5]. Furthermore, a tight lower bound for dimmable VLC systems is proposed in [6], where the capacity formula is in a continuous form as

$$C = \frac{1}{2} W \log_2 \left(1 + w \frac{\rho^2 P^2}{\sigma^2}\right), \tag{12}$$

where $w = e/2\pi$ is a constant with e is the value of the base of natural logarithms. W, ρ, P, and σ^2 denote the modulation bandwidth, the responsivity of the PD, the optical power, and the variance of the Gaussian noise, respectively. Therefore, the SE of the k-th user is given by

$$R_k = \frac{1}{2} \log_2 \left(1 + w\gamma_k\right), \tag{13}$$

where γ_k indicates the individual signal-to-interference-plus-noise ratio (SINR) and can be expressed as

$$\gamma_k = \frac{\rho_k^2 \left\{ \left[\mathbf{H}_k^{(2)} \mathrm{vec}(\mathbf{G}) + \mathbf{h}_k^{(1)} \right]^T \mathbf{P}\mathbf{f}_k \right\}^2}{\sigma_k^2 + \rho_k^2 \sum_{i=1, i\neq k}^{K} \left\{ \mathbf{h}_k^{(1)T} \mathbf{P}\mathbf{f}_i \right\}^2 \mathrm{var}\left(y_i\right)}, \tag{14}$$

where $\mathrm{var}(y_i) = 1$ denotes the variance of the interference signal y_i, and $\sigma_k^2 \in \mathbb{R}_+$ denotes the variance of w_k. In the end, the overall SE is formulated as

$$R = \sum_{k=1}^{K} R_k \left(\mathbf{G}, \mathbf{P}, \mathbf{F}\right). \tag{15}$$

Significantly, this paper focuses on maximizing the overall SE by jointly optimizing the IRS coefficient matrix $\mathbf{G}$, the power allocation matrix $\mathbf{P}$, and the user association matrix $\mathbf{F}$. For the sake of simplicity, the index sets of transmitters, IRS units, and users are denoted by $\mathcal{L}$, $\mathcal{N}$, and $\mathcal{K}$, respectively. Therefore, the optimization problem is formulated as

$$\begin{aligned}
(\mathrm{P}): \ & \max_{\mathbf{G},\mathbf{P},\mathbf{F}} \ R && (16)\\
& \text{s.t. } R_k \geq R_{\min,k}, \quad \forall k \in \mathcal{K}, && (17)\\
& \sum_{l=1}^{L} P_l \leq P_{\text{total}}, && (18)\\
& P_{\min} \leq P_l \leq P_{\max}, \quad \forall l \in \mathcal{L}, && (19)\\
& f_{l,k} \in \{0,1\}, \quad \forall l \in \mathcal{L}, \ k \in \mathcal{K}, && (20)\\
& \sum_{k=1}^{K} f_{l,k} \in \{0,1\}, \quad \forall l \in \mathcal{L}, && (21)\\
& g_{n,l} \in \{0,1\}, \quad \forall n \in \mathcal{N}, \ l \in \mathcal{L}, && (22)\\
& \sum_{l=1}^{L} g_{n,l} \in \{0,1\}, \quad \forall n \in \mathcal{N}. && (23)
\end{aligned}$$

Here the constraint in (17) denotes the individual quality of service (QoS) requirement. The constraint in (18) is the total power limitation and the constraint in (19) is the individual illumination requirement in VLC systems. Then, constraints in (20) and (21) indicate that one transmitter cannot carry information symbols for multiple users simultaneously, while constraints in (22) and (23) result from the definition of the IRS coefficient matrix. Moreover, CSI is denoted by matrices $\mathbf{H}^{(1)}$ and $\mathbf{H}^{(2)}$, which are assumed known by VLC channel estimation techniques.

Algorithm 1 Alternating Optimization Algorithm to Solve (P)

Input: CSI matrices $\mathbf{H}^{(1)}$ and $\mathbf{H}^{(2)}$, constant ϵ_1.
Output: $\mathbf{G}$, $\mathbf{P}$, and $\mathbf{F}$.
1: **Init:** iteration rounds $i \leftarrow 0$, $\mathbf{G}^{(0)}$, $\mathbf{P}^{(0)}$, and $\mathbf{F}^{(0)}$ are a random feasible solution to (P).
2: **repeat**
3: Given $\mathbf{P}^{(i)}$ and $\mathbf{F}^{(i)}$, solve (P1) by variable frozen method and obtain IRS coefficient matrix $\mathbf{G}^{(i+1)}$;
4: Given $\mathbf{G}^{(i+1)}$ and $\mathbf{F}^{(i)}$, solve (P2) by MM algorithm and obtain power allocation matrix $\mathbf{P}^{(i+1)}$;
5: Given $\mathbf{G}^{(i+1)}$ and $\mathbf{P}^{(i+1)}$, solve (P3) by heuristic MM algorithm and obtain user association matrix $\mathbf{F}^{(i+1)}$;
6: **until** $|R^{(i+1)}(\mathbf{G},\mathbf{P},\mathbf{F}) - R^{(i)}(\mathbf{G},\mathbf{P},\mathbf{F})| < \epsilon_1$

Note that the IRS configuration subproblem is structurally identical to the resource allocation problems in orthogonal frequency division multiplexing (OFDM) systems, which is proved to be typically non-deterministic polynomial (NP)-hard [31]. Therefore, the complexity for pursuing the optimal solution of (P) suffers an exponential explosion and it can only search for a suboptimal solution. As a consequence, (P) is split into three subproblems (P1)$\sim$(P3) in **Algorithm 1**, which once optimize a single variable while the other two variables are fixed. Take IRS configuration process as an example, $\mathbf{G}^{(i+1)}$ is defined as $\arg_{\mathbf{G}} \max(R(\mathbf{G}^{(i)}, \mathbf{P}^{(i)}, \mathbf{F}^{(i)}), R(\mathbf{G}_*^{(i)}, \mathbf{P}^{(i)}, \mathbf{F}^{(i)}))$, namely the one with larger SE according to (15), where $\mathbf{G}_*^{(i)}$ is the optimized result of (P1). The above definition is extended to other variables, and therefore, the monotonicity of the

Algorithm 2 Frozen Variable Algorithm to Solve (P1)

Input: fixed matrices $\mathbf{P}$, $\mathbf{F}$ and CSI matrices $\mathbf{H}^{(1)}$ and $\mathbf{H}^{(2)}$.
Output: optimal result $\mathbf{G}$.

Init: $n \leftarrow 1$, $\mathbf{G}^{(0)}$ is a feasible solution.
Construct indication matrices by $\mathbf{H}_k^{(2)}\{\text{supp}(\mathbf{f}_k)\}$;
Compare $h_{k,n,l}^{(2)}$ in the n-th row of the indication matrix and select the column index l^* with the large value;
Freeze variables in other columns of $\mathbf{G}$ and aggregate changeable elements into matrix $\widetilde{\mathbf{G}}$;
Solve (P1-b) by PGD algorithm and obtain the global optimal point $\widetilde{\mathbf{G}}_\dagger$;
Recovery the relaxed result of (P1-a) $\mathbf{G}_\dagger$ with the information of $\mathbf{F}$, $\mathbf{P}$, and $\mathbf{H}_k^{(2)}$;
repeat
  $l_\dagger \leftarrow \arg\min_l g_{n,l}$;
  $g_{n,l_\dagger} \leftarrow 1$ and $g_{n,l\neq l_\dagger} \leftarrow 0$;
  $n \leftarrow n+1$;
until $n > N$

algorithm in the i-th loop is warranted as

$$\begin{aligned} R\left(\mathbf{G}^{(i)},\mathbf{P}^{(i)},\mathbf{F}^{(i)}\right) &\le R\left(\mathbf{G}^{(i+1)},\mathbf{P}^{(i)},\mathbf{F}^{(i)}\right) \\ &\le R\left(\mathbf{G}^{(i+1)},\mathbf{P}^{(i+1)},\mathbf{F}^{(i)}\right) \\ &\le R\left(\mathbf{G}^{(i+1)},\mathbf{P}^{(i+1)},\mathbf{F}^{(i+1)}\right). \end{aligned} \tag{24}$$

It is noted that the overall SE will not decrease in each step since the worse result is discarded. Moreover, the SE is also upper-bounded due to the power constraints in (18) and (19) and row sum constraints in (21) and (23), resulting in its convergence with the progress of iterations.

B. Frozen Variable Algorithm for (P1)

The IRS configuration subproblem is investigated in this part, and the frozen variable algorithm is proposed in **Algorithm 2** to optimize $\mathbf{G}$. To start with, when the power allocation matrix $\mathbf{P}$ and the user association matrix $\mathbf{F}$ are fixed, the original problem (P) is simplified into

$$(\text{P1}): \max_{\mathbf{G}:(17),(22),(23)} \sum_{k=1}^{K} R_k(\mathbf{G}), \tag{25}$$

which is an integer programming problem and NP-hard to solve [31]. To find a suboptimal but effective algorithm, we relax the constraint in (22) to

$$0 \le g_{n,l} \le 1, \tag{26}$$

and rename (P1) as (P1-a). Then, the relaxed problem (P1-a) will be optimized firstly, after which the result can be utilized to obtain the suboptimal point of (P) expediently. A property is derived in the following lemma to simplify the constraint (23).

Lemma 1: $R(\mathbf{G})$ increases monotonically versus $g_{n,l}$.

Proof: Considering the VLC channel gain is naturally real and nonnegative, i.e., $h_{k,n,l}^{(2)} \ge 0$, $\gamma_k(\mathbf{G})$ is a monotone increasing function versus $g_{n,l}$. Therefore, $R(\mathbf{G})$ also increases monotonically versus $g_{n,l}$ since it is a compound function of $\gamma_k(\mathbf{G})$ and $R_k(\gamma_k)$. ■

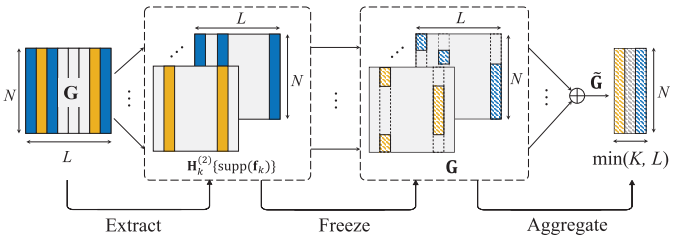

Fig. 3. Three steps to generate $\widetilde{\mathbf{G}}$ from $\mathbf{G}$: variables extraction, frozen, and aggregation.

Based on Lemma 1, the optimal result of (P1) and (P1-a) must lie on the boundary of the constraint (23), which can be rewritten as

$$\sum_{l=1}^{L} g_{n,l} = 1. \tag{27}$$

Till now, the relaxed problem (P1-a) can be solved by abundant optimization algorithms, which are provided in the CVX toolbox [32]. However, the scales of variables and constraints in (P1-a) are proportional to $N \times L$, which heavily increases the computational complexity when L and N are large. Notably, one of the highlights of this paper is to freeze partial variables in (P1-a), by which (P1-a) can be transformed into an equivalent problem with much fewer variables and constraints. As shown in Fig. 3, this transformation exploits the discreteness and row features of matrices $\mathbf{F}$ and $\mathbf{G}$ to generate a reduced variable $\widetilde{\mathbf{G}}$, detailed discussions are given as follows.

- **Extract:** This step aims to select the corresponding variables for each user and divide them into K disjoint sets. According to (8), the variable $g_{n,l}$ can make contributions to R_k if and only if the index l lies in the space of $\text{supp}(\mathbf{f}_k)$. Therefore, the elements in $\mathbf{G}\{\text{supp}(\mathbf{f}_k)\}$ form a variable set, which is disjoint with other sets due to the orthogonality of $\mathbf{f}_k$.
- **Freeze:** In this step, some variables in the k-th set will be fixed as zeros, while other ones remain changeable to be optimized. Specifically, the location of the largest element $h_{k,n,l}^{(2)}$ in each row of $\mathbf{H}_k^{(2)}\{\text{supp}(\mathbf{f}_k)\}$ is selected, and then the variable at the corresponding location remains unfrozen. At the same time, other elements in that row of $\mathbf{G}\{\text{supp}(\mathbf{f}_k)\}$ are to be zeros, which reduces the numbers of variables and constraints together.
- **Aggregate:** After the above two processes, only N elements of each set are still changeable. To maintain the structure of variables, this step vectorizes the variables in different sets and aggregates them into a new matrix $\widetilde{\mathbf{G}}$, and its column rank is given by

$$\text{rank}^{(c)}\left(\widetilde{\mathbf{G}}\right) = \min(K, L). \tag{28}$$

In this way, the dimensions of variables and constraints is decreased from NL to $N\min(K,L)$, which significantly reduces the computational complexity when $K \ll L$.

These operations correspond to steps 2∼4 in **Algorithm 2**, which perform as the basis of the frozen variable algorithm. Then, (P1-a) is transformed into the following form

$$\text{(P1-b)}: \max_{\widetilde{\mathbf{G}}:(17),(26),(27)} \sum_{k=1}^{K} R_k\left(\widetilde{\mathbf{G}}\right). \tag{29}$$

Proposition 1: The optimal result of problem (P1-a) is equivalent to that of (P1-b).

Proof: Suppose the summation of $\sum_{l\in\text{supp}(\mathbf{f}_k)} g_{n,l}$ is limited by constant $c_{n,k}$, the SINR can be rewritten as

$$\gamma_k \leq \frac{\left\{\sum_{l=1}^{L} P_l f_{l,k} h_{k,l}^{(1)} + \sum_{n=1}^{N} c_{n,k} \max\limits_{l\in\text{supp}(\mathbf{f}_k)} \left(P_l h_{k,n,l}^{(2)}\right)\right\}^2}{\sigma_k^2/\rho_k^2 + \sum_{i=1,i\neq k}^{K} \{\mathbf{h}_k^{(1)T}\mathbf{P}\mathbf{f}_i\}^2}, \tag{30}$$

where the equality holds under the condition $g_{n,l^\dagger} = c_{n,k}$ with $l^\dagger = \arg\max_{l\in\text{supp}(\mathbf{f}_k)} P_l h_{k,n,l}^{(2)}$, and the other variables $g_{n,l\neq l^\dagger}$ are zeros. Considering the orthogonality among the columns of $\mathbf{F}$ as

$$\mathbf{f}_i\mathbf{f}_j^T = 0, \quad \forall i \neq j, \tag{31}$$

the sets supp $(\mathbf{f}_k)$ are disjoint with each other and the process of maximizing $R(\mathbf{G})$ is independent among different users. Therefore, the steps of extracting and freezing variables will not lose optimal feasible solutions, which proves the sufficiency of Proposition 1. On the other hand, when the optimal result of (P1-b) is obtained, the corresponding optimal solution to (P1-a) can be reconstructed conversely due to the linearity of transformation in Fig. 3. ∎

Briefly, the relationship between the optimal results of (P1-a) and (P1-b) can be expressed by the following formula:

$$\mathbf{G}^*_{\text{(P1-a)}} \underset{\mathbf{F},\ \mathbf{P},\ \mathbf{H}^{(2)}}{\overset{\mathbf{F},\ \mathbf{P},\ \mathbf{H}^{(2)}}{\Longleftrightarrow}} \widetilde{\mathbf{G}}^*_{\text{(P1-b)}}. \tag{32}$$

Proposition 2: The objective function in (P1-b) is concave when $\gamma_k \gg 2\pi/e$, and the concavity of the subproblem holds asymptotically with the increase of SINR.

Proof: To investigate the concavity of overall SE with respect to $\widetilde{\mathbf{G}}$, the concavity property of $R_k(\mathbf{G})$ is studied firstly and its general Hessian matrix expression is denoted by $\mathbf{H}_{\mathcal{G}}^{(k)} = [\mathcal{G}_{(n_1,n_2,l_1,l_2)}^{(k)}]_{NL\times NL}$, where each element represents the second-order derivative and can be expressed as

$$\begin{aligned}
&\mathcal{G}_{(n_1,n_2,l_1,l_2)}^{(k)} \\
&= \frac{\partial}{\partial g_{n_2,l_2}}\left\{\frac{\gamma_k}{2\pi/e+\gamma_k}\frac{P_{l_1} f_{l_1,k} h_{k,n_1,l_1}^{(2)}/\ln 2}{\left[\mathbf{H}_k^{(2)}\text{vec}(\mathbf{G})+\mathbf{h}_k^{(1)}\right]^T\mathbf{P}\mathbf{f}_k}\right\} \\
&\simeq \frac{\partial}{\partial g_{n_2,l_2}}\left\{\frac{P_{l_1} f_{l_1,k} h_{k,n_1,l_1}^{(2)}/\ln 2}{\left[\mathbf{H}_k^{(2)}\text{vec}(\mathbf{G})+\mathbf{h}_k^{(1)}\right]^T\mathbf{P}\mathbf{f}_k}\right\} \\
&= \frac{-P_{l_1} f_{l_1,k} h_{k,n_1,l_1}^{(2)} P_{l_2} f_{l_2,k} h_{k,n_2,l_2}^{(2)}}{\left\{\left[\mathbf{H}_k^{(2)}\text{vec}(\mathbf{G})+\mathbf{h}_k^{(1)}\right]^T\mathbf{P}\mathbf{f}_k\right\}^2 \ln 2},
\end{aligned} \tag{33}$$

where $\simeq$ denotes the symbol of asymptotic equal and the relationship in the second line holds due to the general condition $\gamma_k \gg 2\pi/e$ in VLC. Given the structure of the formula in (33), the Hessian matrix of the k-th user is written as

$$\mathbf{H}_{\mathcal{G}}^{(k)} = \frac{-\mathbf{a}\mathbf{a}^T}{\left\{\left[\mathbf{H}_k^{(2)}\text{vec}(\mathbf{G})+\mathbf{h}_k^{(1)}\right]^T\mathbf{P}\mathbf{f}_k\right\}^2 \ln 2}, \tag{34}$$

where the introduced vector $\mathbf{a} \in \mathbb{R}_+^{NL\times 1}$ is given by

$$\mathbf{a} = \oplus_{l=1}^{L}\left(P_l f_{l,k}\mathbf{I}_N\right)\text{vec}\left(\mathbf{h}_{k,1}^{(2)}, \mathbf{h}_{k,2}^{(2)}, \ldots, \mathbf{h}_{k,L}^{(2)}\right). \tag{35}$$

It is observed that the Hessian matrix is a rank-one matrix and the inequality $z^T\mathbf{H}_{\mathcal{G}}^{(k)}z \leq 0$ ensures for any vector $z \in \mathbb{R}^{NL\times 1}$. When the condition $\gamma_k \gg 2\pi/e$ holds, $\mathbf{H}_{\mathcal{G}}^{(k)}$ is negative semidefinite, and therefore $R(\mathbf{G})$ is a concave function. Considering $\widetilde{\mathbf{G}}$ lies in the subspace projected by $\mathbf{G}$, $R(\widetilde{\mathbf{G}})$ is also concave under that condition, leading to the fact that (P1-b) is asymptotically a convex problem with the increase of SINR γ_k. ∎

In this way, the relaxed problem (P1-a) is equivalently transformed into an asymptotical convex problem (P1-b), with the numbers of variables and constraints reduced to $\min(1, K/L)$ times of those in (P1-a). Given the assumption $K \ll L$, (P1-b) has far lower computational complexity than (P1-a) to be solved in an instantaneous system. Typically, convex problems can be optimized by directly solving Karush-Kuhn-Tucker (KKT) equations [33]. The closed-form result can be obtained in this algorithm, e.g., the water-filling algorithm and algorithms in [33], providing low optimization complexity. However, a strict requirement for the problem structure is needed, which limits its popularity in problems with complex structure and extensive inequality constraints. The gradient descend algorithm can also be utilized to optimize (P1-b), but its convergence time will be too long when the condition number of the Hessian matrix is large [34]. This section herein chooses the projected gradient descent (PGD) algorithm, which is widely used in convex optimization to accelerate convergence [35]. After obtaining the optimal result of (P1-b), the solution to (P1-a) can be achieved according to (32). This inverse transformation is linear and fast under the given matrices $\mathbf{F}$, $\mathbf{P}$, and $\mathbf{H}_k^{(2)}$. Finally, in steps 7∼11 of **Algorithm 2**, a greedy policy is adopted to recover the discreteness of $\mathbf{G}$ and achieve the suboptimal result of (P1).

C. Minorization-Maximization Algorithm for (P2) and (P3)

1) Power Allocation Problem: When the IRS coefficient matrix $\mathbf{G}$ and the user association matrix $\mathbf{F}$ are determined, the original problem (P) can be reformulated as

$$\text{(P2)}: \max_{\mathbf{P}:(17),(18),(19)} \sum_{k=1}^{K} R_k\left(\mathbf{P}\right), \tag{36}$$

which is proved to be non-convex according to Appendix V and is intractable to search for the optimal result. Generally, a powerful tool to solve non-convex problems is the successive convex approximation (SCA) method, which is realized by optimizing a series of approximate convex problems [36].

As one of the SCA methods, the MM algorithm has been widely used in signal processing, communications and networking, and machine learning [37]. In this paper, we exploit the MM algorithm to solve (P2), and more detailed discussions are provided in the sequel.

In mathematics, the MM algorithm devotes to solving a series of approximate convex problems iteratively, and its key lies in the way of objective function approximation. For any given point of the problem (P2), the MM algorithm requires a lower bound function with as little gap as possible, i.e., a tangent function is the best. In the considered SE maximization problem, this lower bound function has to be concave so that convex optimization algorithms can be used. To this end, we denote the SE function as $\mathfrak{T}^{(1)}(x) = 1/2\log_2(1+x)$ with x the individual SINR, and a function named $\mathfrak{R}^{(1)}(x; x_1^*)$ is given by [38]

$$\mathfrak{R}^{(1)}\left(x; x_1^*\right) = \eta\left(x_1^*\right)\log_2\left(x\right) + \xi\left(x_1^*\right), \tag{37}$$

where x_1^* is a parameter, η and ξ are two functions with respect to x_1^* as

$$\eta\left(x\right) = \frac{x}{2\left(1+x\right)}, \tag{38}$$

$$\xi\left(x\right) = \frac{1}{2}\log_2\left(1+x\right) - \frac{x}{2\left(1+x\right)}\log_2\left(x\right). \tag{39}$$

Then, the following properties are fulfilled for $\mathfrak{R}^{(1)}(x; x_1^*)$:

- It can be proved that the minimum value of $\mathfrak{T}^{(1)}\left(x\right) - \mathfrak{R}^{(1)}\left(x; x_1^*\right)$ obtains at $x = x_1^*$, and the following inequality ensures for any $x \in \mathbb{R}_+$:

$$\mathfrak{T}^{(1)}\left(x\right) \;\geq\; \mathfrak{R}^{(1)}\left(x; x_1^*\right). \tag{40}$$

- At the point of x_1^*, two functions have the same value as

$$\mathfrak{T}^{(1)}\left(x_1^*\right) \;=\; \mathfrak{R}^{(1)}\left(x_1^*; x_1^*\right). \tag{41}$$

- The tangent slope of two functions can be obtained by calculating the first derivatives as

$$\frac{\partial \mathfrak{T}^{(1)}\left(x\right)}{\partial x}|_{x=x_1^*} \;=\; \frac{\partial \mathfrak{R}^{(1)}\left(x; x_1^*\right)}{\partial x}|_{x=x_1^*}. \tag{42}$$

Consequently, the function $\mathfrak{T}^{(1)}(x)$ is tightly lower bounded by $\mathfrak{R}^{(1)}(x; x_1^*)$ with x_1^* the tangent point, and the SE function $R_k(\mathbf{P}) = \mathfrak{T}^{(1)}(w\gamma_k(\mathbf{P}))$ is bounded by the approximate function $\mathfrak{R}^{(1)}(w\gamma_k(\mathbf{P}); x_1^*)$, where $x_1^* = w\gamma_k(\mathbf{P}^{(t)})$ denotes the tangent point in the t-th loop. This approximate function is renamed as $f_k^{(1)}(\mathbf{P}; \mathbf{P}^{(t)})$ for simplicity. Unfortunately, it has been proved to be non-convex in Appendix V, and therefore the requirements of the MM algorithm is not met.

Nevertheless, making one more approximation is reasonable here since the gap between the $\mathfrak{T}^{(1)}(x)$ and $\mathfrak{R}^{(1)}(x; x_1^*)$ is extremely negligible, even if far from the tangent point [38]. Specifically, we further rewrite $f_k^{(1)}(\mathbf{P}; \mathbf{P}^{(t)})$ by expanding the numerator and denominator in the logarithmic function, and an approximation function is introduced as

$$\mathfrak{R}^{(2)}\left(x; x_2^*\right) = \log_2\left(x_2^*\right) + \left(x/x_2^* - 1\right)/\ln 2, \tag{43}$$

which is the first-order Taylor expansion of the function $\mathfrak{T}^{(2)}(x) = \log_2(x)$ with x_2^* the tangent point [39]. Then, the subtracted Logarithmic term in $f_k^{(1)}(\mathbf{P}; \mathbf{P}^{(t)})$ can be substituted by the Taylor expansion, leading to a much lower bound as

$$\begin{aligned} &f_k^{(2)}\left(\mathbf{P}; \mathbf{P}^{(t)}\right) \\ &= 2\eta\left(x_1^*\right)\log_2\left(\left[\mathbf{H}_k^{(2)}\mathrm{vec}(\mathbf{G}) + \mathbf{h}_k^{(1)}\right]^T \mathbf{P}\mathbf{f}_k\right) \\ &\quad + \xi\left(x_1^*\right) - \eta\left(x_1^*\right) \\ &\quad \times \mathfrak{R}^{(2)}\left(\sigma_k^2 + \rho_k^2 \sum_{i=1, i\neq k}^{K}\left\{\mathbf{h}_k^{(1)T}\mathbf{P}\mathbf{f}_i\right\}^2; x_2^*\right) \\ &\quad + \eta\left(x_1^*\right)\log_2\left(w\rho_k^2\right), \end{aligned} \tag{44}$$

where the tangent point is denoted by $x_2^* = \sigma_k^2 + \rho_k^2 \sum_{i=1, i\neq k}^{K}\{\mathbf{h}_k^{(1)T}\mathbf{P}^{(t)}\mathbf{f}_i\}^2$. According to the characteristics of the first-order Taylor expansion, the local and global properties similarly to (40)-(42) also hold for $f_k^{(2)}(\mathbf{P}; \mathbf{P}^{(t)})$, and a partial order relation is ensured as

$$f_k^{(2)}\left(\mathbf{P}; \mathbf{P}^{(t)}\right) \leq f_k^{(1)}\left(\mathbf{P}; \mathbf{P}^{(t)}\right) \leq R_k\left(\mathbf{P}\right). \tag{45}$$

Lemma 2: $f_k^{(1)}\left(\mathbf{P}; \mathbf{P}^{(t)}\right)$ and $f_k^{(2)}\left(\mathbf{P}; \mathbf{P}^{(t)}\right)$ are non-concave and concave functions, respectively.

Proof: The derivation is given in Appendix V. ∎

By now, two lower bounds of the SE function $R_k(\mathbf{P})$ have been given, where the latter one is a concave function. Considering requirements of the MM algorithm, the objective in (P2) is replaced by $f_k^{(2)}(\mathbf{P}; \mathbf{P}^{(t)})$, and the transformed subproblem can be expressed as

$$\text{(P2-a)}: \max_{\substack{\mathbf{P}:(18),(19) \\ f_k^{(2)}\left(\mathbf{P}; \mathbf{P}^{(t)}\right) \geq R_{\min,k}}} \quad \sum_{k=1}^{K} f_k^{(2)}\left(\mathbf{P}; \mathbf{P}^{(t)}\right). \tag{46}$$

Proposition 3: (P2-a) is a convex problem.

Proof: The constraint of the replaced QoS requirement is convex due to Lemma 2, and the constraints in (18) and (19) are linear. Moreover, the objective function is concave since it is the summation of K concave functions, leading to the convexity of the subproblem (P2-a). ∎

As illustrated in **Algorithm 3**, the problem (P2) is solved by optimizing a series of approximate convex problems iteratively. Taking the t-th loop as an example, (P2) is replaced by (P2-a) firstly, which is proved to be a convex problem in Proposition 3. Therefore, the KKT conditions of (P2-a) will always be satisfied unless the feasible space is an empty set. Then, the PGD algorithm can be utilized in step 4 to solve the convex problem (P2-a) [35], where the optimal result is denoted by $\mathbf{P}^{(t)}$. Once the result $\mathbf{P}^{(t)}$ is obtained, the tangent points $x_1^{*(t+1)}$ and $x_2^{*(t+1)}$ and the related parameters can be calculated. The iteration will continue until the convergence condition $\|\mathbf{P}^{(t+1)} - \mathbf{P}^{(t)}\|_F < \epsilon_2$ is met, where ϵ_2 is a given threshold.

2) User Association Problem: Given the IRS coefficient matrix $\mathbf{G}$ and power allocation matrix $\mathbf{P}$, the problem (P) is transformed into user association problem, which is given by

$$\text{(P3)}: \max_{\mathbf{F}:(17),(20),(21)} \quad \sum_{k=1}^{K} R_k\left(\mathbf{F}\right). \tag{47}$$

Algorithm 3 MM Algorithm to Solve (P2)

Input: Fixed parameters $\mathbf{F}$, $\mathbf{G}$, and ϵ_2, and CSI matrices $\mathbf{H}^{(1)}$ and $\mathbf{H}^{(2)}$.

Output: suboptimal $\mathbf{P}$.

Init: iteration rounds $t \leftarrow 0$, and $x_1^{*(0)}$, $\eta(x_1^{*(0)})$, $\xi(x_1^{*(0)})$, $x_2^{*(0)}$ are initialized, respectively.
repeat
  $t \leftarrow t+1$, $k \leftarrow 1$;
  Solve (P2-a) by the PGD algorithm and find the power allocation matrix $\mathbf{P}^{(t)}$;
  repeat
    $x_1^{*(t)} \leftarrow w\gamma_k(\mathbf{P}^{(t)})$;
    $\eta(x_1^{*(t)})$ is calculated based on (38);
    $\xi(x_1^{*(t)})$ is calculated based on (39);
    $x_2^{*(t)} \leftarrow \sigma_k^2 + \rho_k^2 \sum_{i=1,i\neq k}^{K} \{\mathbf{h}_k^{(1)T}\mathbf{P}^{(t)}\mathbf{f}_i\}^2$;
    $k \leftarrow k+1$;
  until $k > K$
until $\|\mathbf{P}^{(t+1)} - \mathbf{P}^{(t)}\|_F < \epsilon_2$

To start with, the constraint in (20) is relaxed as $0 \le f_{l,k} \le 1$, which can be regarded as the service probability of the k-th user provided by the l-th transmitter. Then, according to the definition of the individual SINR in (14), the objective function $R_k(\mathbf{F})$ has a similar structure with $R_k(\mathbf{P})$, which indicates that the relaxed form of (P3) is also a non-convex problem. Therefore, the MM algorithm is appropriate to solve (P3), and the detailed process has been elaborated in the power allocation problem (P2). Notably, the result of the MM algorithm is a continuous variable. To maintain the correctness of the constraint (20), we can directly force the largest element in each row to 1 while other elements are zeros. Considering the similarity of (P2) and (P3), the proof of related properties and the descriptions of the algorithm are ignored here.

D. Discussions on Extremely Weak/Severe Interferences

Though the proposed MM algorithm can deal with non-convex problems well, the process of optimizing a series of subproblems still suffers from considerable computational complexity. In this subsection, we re-examine the power allocation problem and **Algorithm 3**, aiming to simplify the optimization processes in the extremely weak/severe interference regimes.

1) Extremely Weak Interference: Generally, weak interference refers to cases such as extreme low emission power or the user is exactly under the LED. For both situations the inter-lamp interferences for an individual user is faint, and therefore the denominator term of (14) is dominated mainly by the AWGN noise. Specifically, R_k is asymptotically rewritten as

$$R_k^{(L)} = \frac{1}{2}\log_2\left(1 + \frac{w\rho_k^2}{\sigma_k^2}\left\{\left[\mathbf{H}_k^{(2)}\mathrm{vec}(\mathbf{G}) + \mathbf{h}_k^{(1)}\right]^T \mathbf{P}\mathbf{f}_k\right\}^2\right) \simeq \frac{w\rho_k^2}{2\sigma_k^2 \ln 2}\left\{\left[\mathbf{H}_k^{(2)}\mathrm{vec}(\mathbf{G}) + \mathbf{h}_k^{(1)}\right]^T \mathbf{P}\mathbf{f}_k\right\}^2, \quad (48)$$

where the approximation ensures by setting the tangent point of (43) to 1. Based on (31), the SE functions $R_k^{(L)}$ are independent to each other, and these K objective functions are related by power constraints in (18) and (19). Moreover, the problem aims to maximize a convex function (48) in a convex feasible space, which demonstrates that the optimal point must be at the boundary of the feasible space, resulting in the maximum of $R_k^{(L)}$ as

$$R_k^{(L)} \le R_{\max,k}^{(L)} = \frac{w\rho_k^2}{2\sigma_k^2 \ln 2}\Bigg\{\sum_{\substack{l\in\mathrm{supp}(\mathbf{f}_k),\\ l\neq l_\dagger^{(k)}}}\left(\mathbf{h}_{k,l}^{(2)T}\mathbf{g}_l + h_{k,l}^{(1)}\right)P_{\min} + \max\left(\sum_{l\in\mathrm{supp}(\mathbf{f}_k)} P_l - (|\mathrm{supp}(\mathbf{f}_k)|-1)P_{\min}, P_{\min}\right) \times \left(\mathbf{h}_{k,l_\dagger^{(k)}}^{(2)T}\mathbf{g}_{l_\dagger^{(k)}} + h_{k,l_\dagger^{(k)}}^{(1)}\right)\Bigg\}^2, \quad (49)$$

where $l_\dagger^{(k)}$ denotes the index of LED with the largest power, and is given by

$$l_\dagger^{(k)} = \arg\max_{l\in\mathrm{supp}(\mathbf{f}_k)}\left(\mathbf{h}_{k,l}^{(2)T}\mathbf{g}_l + h_{k,l}^{(1)}\right). \quad (50)$$

Then, the power allocation problem under weak interference assumption can be expressed as

$$\text{(P2-b)}: \max_{\mathbf{P}:(18),P_l\ge P_{\min}} \sum_{k=1}^{K} R_{\max,k}^{(L)}(\mathbf{P}), \quad (51)$$

where the maximum illumination requirement $P_l \le P_{\max}$ is assumed satisfied in advance. Though (P2-b) is a non-convex problem, the facts that the feasible space is a polyhedron and the objective is convex simplify the problem dramatically, i.e., we can check and compare the function values at corners of the polyhedron. By replacing each variable P_l with $\beta_l = P_l - P_{\min}$, the above problem is transformed equivalently as

$$\text{(P2-c)}: \max_{\substack{\boldsymbol{\beta}:\ \beta_l\ge 0,\\ \sum_{l=1}^{L}\beta_l \le P_{\text{total}} - LP_{\min}}} \sum_{k=1}^{K} R_{\max,k}^{(L)}(\boldsymbol{\beta}). \quad (52)$$

The corner of (P2-c) has a general form of $\beta_l = P_{\text{total}} - LP_{\min}$ for a specific l while other variables are zeros. Conversely, the global optimal result of (P2-b) is $P_{l_\dagger^{(k)}} = P_{\text{total}} - (L-1)P_{\min}$ for one user, and other emission power are all $P_{\min}$. The number of comparisons equals the number of corners of the polyhedron, i.e., the complexity is $\mathcal{O}(L)$.

2) Extremely Severe Interference: The severe interference corresponds to the cases such as high emission power or the user is located at the overlapping area of multiple LEDs. In these circumstances, the noise power is negligible to the inter-lamp interferences, and consequently the interference term dominates the denominator of (14). More specifically, the individual SINR of the k-th user can be expressed as

$$\gamma_k^{(H)}(\mathbf{P}) \simeq \frac{\left\{\left[\mathbf{H}_k^{(2)}\mathrm{vec}(\mathbf{G}) + \mathbf{h}_k^{(1)}\right]^T \mathbf{P}\mathbf{f}_k\right\}^2}{\sum_{i=1,i\neq k}^{K}\left\{\mathbf{h}_k^{(1)T}\mathbf{P}\mathbf{f}_i\right\}^2}. \quad (53)$$

Notably, it can be observed that the power allocation policy among transmitters is important, while the absolute emission power will not affect the achievable SE at all, i.e., $\gamma_k(\mathbf{P}) = \gamma_k(a\mathbf{P})$ with any real and positive number a. This is because the growth of emission power will increase the MUIs and the power of effect signals simultaneously in the severe interference regimes. Particularly, allocating all emission power with $P_{\min}$ will lead to the same overall SE as the case of $P_{\max}$, namely $\gamma_k(\mathbf{P}_{\min}) = \gamma_k(\mathbf{P}_{\max})$, where $\mathbf{P}_{\min}$ and $\mathbf{P}_{\max}$ are the results of identical matrices multiplied by $P_{\min}$ and $P_{\max}$, respectively.

E. Computational Complexity Analysis

This section discusses the computational complexity of the proposed algorithms. The analysis is performed firstly on the frozen variable algorithm and the MM algorithm, and then the complexity of the overall algorithm is provided. To be clear, an operation corresponds to one time of iteration, and the content of each algorithm is split into segments.

1) The Frozen Variable Algorithm for (P1): The discussion on the complexity of **Algorithm 2** includes the following aspects:

- Extract and freeze variables: Step 2 generates K support sets according to the columns of $\mathbf{F}$, leading to $\mathcal{O}(KL)$ operations. Then, steps 3∼4 compare the elements in the indication matrix, which require $\mathcal{O}(KN\max(L-K,0))$ comparisons;
- Solve (P1-b) by the PGD algorithm: According to [35], the number of iterations for PGD algorithm to converge is $\mathcal{O}(1/\epsilon)$, where ϵ is a given error threshold;
- Discreteness recovery: Steps 7∼11 require the operations of $\mathcal{O}(NL)$.

2) The MM Algorithm for (P2) and (P3): The analysis on the complexity of **Algorithm 3** is provided as follows:

- Solve (P2-a) by the PGD algorithm: When the condition $2K \geq L$ ensures, the Hessian matrix $\mathbf{H}_{\mathcal{P}}$ is full-rank and the objective function is m^o-strongly concave according to (67). Then, the number of iterations to be converged is $\mathcal{O}(\log(1/\epsilon))$ with ϵ the error threshold. Nevertheless, we have $\mathrm{rank}(\mathbf{H}_{\mathcal{P}}) < \mathrm{rank}(\mathbf{P})$ when $2K < L$, leading to $\mathcal{O}(1/\epsilon)$ iterations for the PGD algorithm to converge [35];
- Parameters update: The parameters of $f_k^{(2)}\left(\mathbf{P};\mathbf{P}^{(t)}\right)$ are updated in steps 5∼11, including $x_1^{*(t)}$, $\eta(x_1^{*(t)})$, $\xi(x_1^{*(t)})$, $x_2^{*(t)}$, which require $4K$ operations;
- Function approximation: Assume the number of function approximations is T, at least $\mathcal{O}(T\log(1/\epsilon))$ iterations are needed for the PGD algorithm to converge and $\mathcal{O}(4TK)$ operations are desired to update the parameters. As for (P3), KL more operations are needed to force the relaxed result to be discrete.s

3) Overall Algorithm for (P): **Algorithm 1** is composed of three main steps, namely the frozen variable algorithm for (P1) and the MM algorithm for (P2) and (P3). As for the former algorithm, though the objective function is not a strong concave function, the variable freeze process reduces the numbers of elements and constraints from LN to $N\min(K,L)$. Moreover, the PGD algorithm takes only once in (P1). On the other hand, a series of convex approximation problems are optimized in the MM algorithm. However, the strong concavity of the objective function provides a faster convergence rate when $2K > L$, and therefore the computational complexity has been balanced between step 3 and steps 4∼5 of the overall algorithm.

TABLE II
SIMULATION PARAMETERS

Parameter	Value
The Lambertian index, m	1
The optical filter gain, g_{of}	1
The FoV of the concentrator, Φ	70°
The PD area, A	1 cm^2
The internal refractive index, q	1.5
PD responsivity, ρ_k	0.5 A/W
The area of the IRS unit, D_0	10 cm × 10 cm
L, K, N	4, 4, 128
The power of Gaussian noise, σ^2	10^{-8} W
The reflection factor, δ	0.9
Minimum QoS requirments, $R_{\min,k}$	0.02 bps/Hz
$P_{\min}$, $P_{\max}$, P_{total}	3 W, 7 W, 20 W

IV. NUMERICAL RESULTS

The performance of the IRS-aided indoor multi-user VLC system is evaluated in this section. Without loss of generality, the room size is 8 m × 8 m × 3 m, and four LEDs are evenly distributed on the roof with the locations at (2 m, 2 m, 3 m), (2 m, 6 m, 3 m), (6 m, 2 m, 3 m), and (6 m, 6 m, 3 m). All PDs are randomly distributed on the plane 1 m above the ground, which is divided into 100 × 100 equidistant meshes. Then, an IRS is deployed on one wall of the room, and all units are evenly scattered within the rectangle area with (0 m, 1 m, 1.5 m) and (0 m, 7 m, 2.5 m) as corners. More detailed parameters are shown in Table II, and they will not be changed in the sequel without special instructions. In general, various numerical simulations are carried out to show the effectiveness of IRS-aided VLC, including the comparisons among the proposed algorithms and other baselines, the influence of several important parameters, and also the geometric factors such as the room size and the locations of IRS.

A. Simulations on the Proposed Algorithms

In this subsection, the proposed **Algorithm 2** and **Algorithm 3** that focus on the IRS configuration subproblem and the power allocation subproblem are examined separately by comparing with other baselines. To start with, the comparisons among different IRS configuration schemes are shown in Fig. 4, where the irrelevant variables $\mathbf{P}$ and $\mathbf{F}$ of all baselines are optimized in the same way as **Algorithm 1**. It is supposed that the NLoS channel of each user is blocked by a homogeneous media with a probability of 50%, which is modeled by a multiplicative factor of 0.3. For comparison, the result under the relaxed constraint (26) and the one

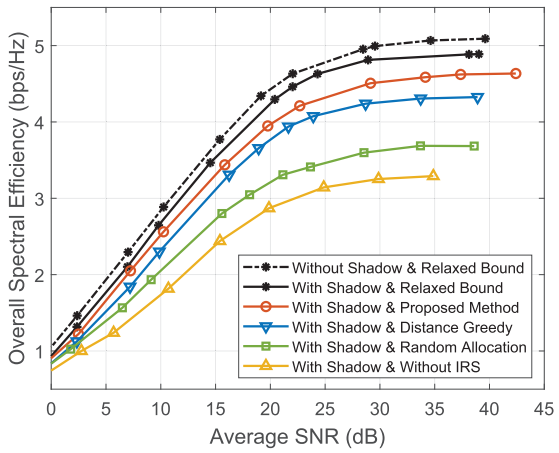

Fig. 4. IRS configuration: the overall SE versus the average SNR (dB) with different IRS configuration policies.

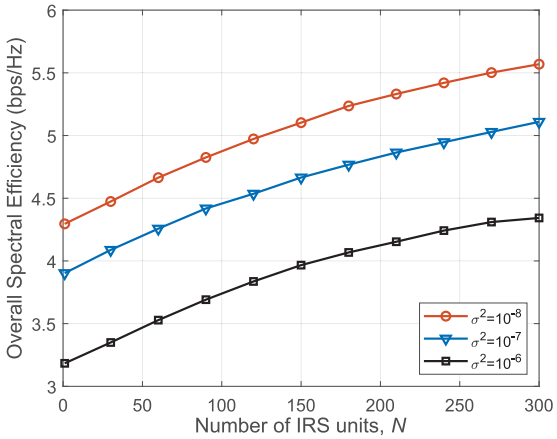

Fig. 6. The overall SE versus the number of IRS units with different Gaussian noise powers $\sigma^2 = 10^{-8}$, 10^{-7}, and 10^{-6} W.

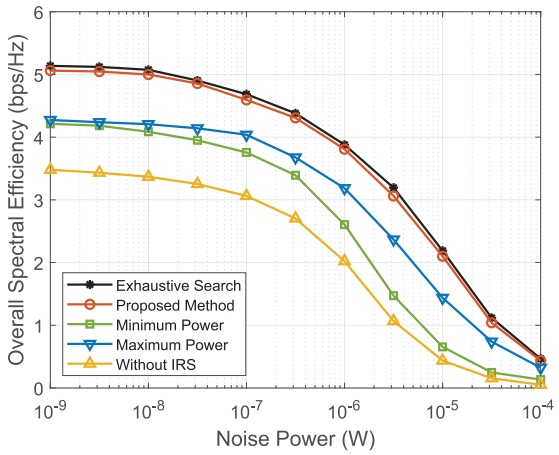

Fig. 5. Power allocation: the overall SE versus the Gaussian noise power with different power allocation policies.

without IRS are chosen as the upper bound and lower bound, respectively. Then, the distance greedy policy that allocates each unit to the nearest transmitter and the random allocation policy on **G** are also baselines. As shown in the results, the SE of each policy converges to a value with the growth of the average signal-to-noise ratio (SNR), and the proposed frozen variable algorithm achieves more SE than other baselines, e.g., more than 1 bps/Hz gain to the lower bound in the high SNR regimes. Therefore, IRS can increase the overall SE to mitigate the effects of occlusion in VLC, and the proposed configuration algorithm achieves more gain than other baselines.

On the other hand, Fig. 5 verifies the effectiveness of the proposed power allocation policy on optimizing **P**, and every scheme adopts the same policy in **Algorithm 1** to obtain the unconcerned variables **G** and **F**. To this end, the exhaustive search method and no IRS result are considered as upper and lower bounds, respectively. More specifically, the interval of emission power $P_l \in (P_{\min}, P_{\max})$ is divided into 100 equal slices in the former case, and then all possible power allocation combinations of four LEDs are checked to obtain the optimal result. Another two fixed power baselines include the maximum power allocation and the minimum power allocation schemes, which assign P_{total}/L and $P_{\min}$ as the emission power, respectively. Though (P2) is not a convex problem, it is observed that the SE gap between the proposed power allocation policy and the upper bound is limited, which can attribute to the fact that the MM algorithm avoids falling into the local optimal point. Secondly, the SE gain between the no IRS scheme and the proposed algorithm exceeds 1.5 bps/Hz when the noise power is 10^{-9}, and even 0.7 bps/Hz can be achieved for the minimum power allocation scheme. Finally, the numerical results also show that two fixed power schemes almost share the same SE performance in weak interference conditions, which is consistent with the theoretical analysis in Section III-D.

B. Simulations on Important Parameters

Next, we investigate the influence of some important parameters on the SE performance, where the optimizations of **G**, **P**, and **F** are executed by **Algorithm 1**. Notably, the NLoS channel gain in this paper is based on the point source assumption, which requires a sufficiently large area for each IRS unit. Considering the predefined area for IRS is 6 m $\times$ 1 m and the unit area is 10 cm $\times$ 10 cm, the unit spacing is about 2.5 cm if the number of units is 300. As shown in Fig. 6, the overall SE increases almost linearly versus the number of IRS units when $N \leq 300$. Moreover, once N increases larger than 300, the point source assumption is violated and the formula (5) is no longer right, which is beyond the scope of this paper.

Then, the effect of reflection factor δ is shown in Fig. 7. Specifically, the number of IRS units changes from 4 to 256, and the no IRS result performs as the lower bound. It is observed that the overall SE increases versus the reflection factor in a linear form, where the slope depends heavily on the number of IRS units. For example, it needs $\delta = 0.7$ for the $N = 64$ situation to achieve 4.6 bps/Hz while the only $\delta = 0.2$ is needed for the $N = 256$ situation. Therefore, the number of IRS units and the reflection factor are two types

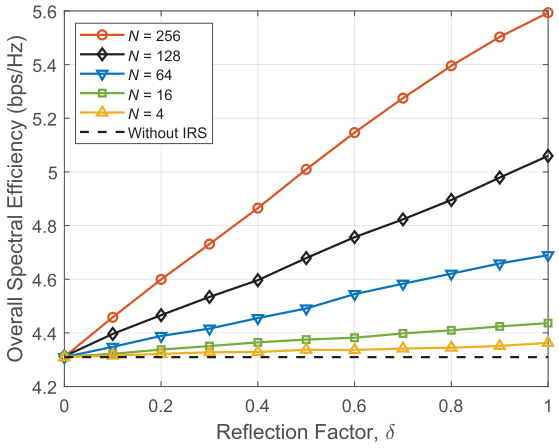

Fig. 7. The overall SE versus the reflection factor with the different numbers of IRS units.

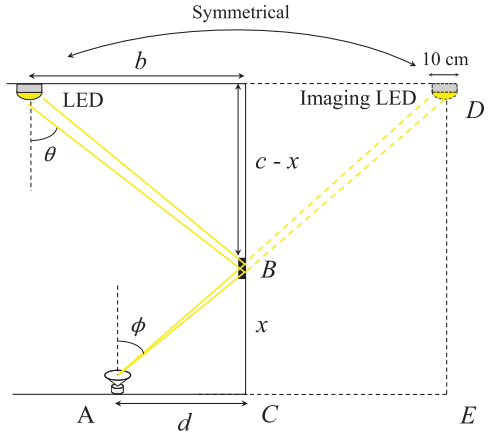

Fig. 8. A two-dimensional geometrical diagram of IRS deployment.

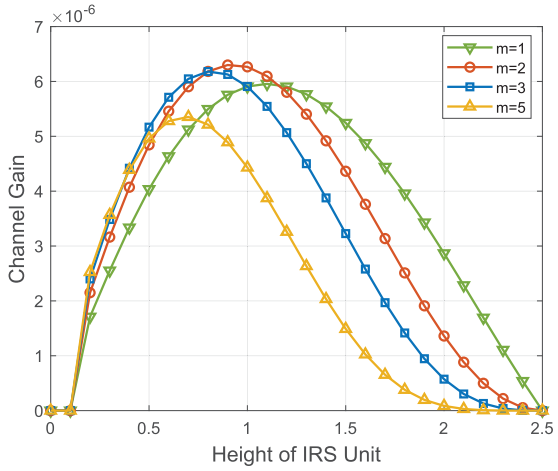

Fig. 9. NLoS channel gain versus the height of IRS unit with different Lambertian index.

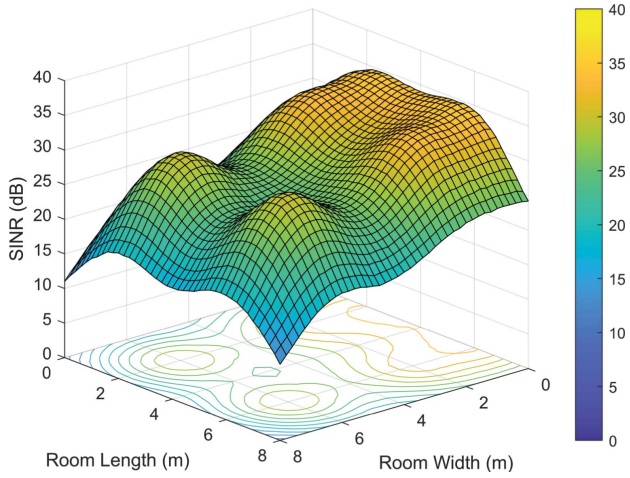

Fig. 10. SINR performance when the room size is 8 m × 8 m × 3 m, and an IRS is deployed on one wall.

of resources that need to be balanced, which provides a guide for applications of VLC IRS.

C. Simulations on Geometric Factors of IRS

Considering that the indoor VLC channel gain highly depends on the geometric factors of transceivers and reflectors, this subsection validates these influences from three different aspects, including the minimum area of PD, the deployment height of IRS unit, and the size of room. To start with, a two-dimensional diagram is provided in Fig. 8 with the height of the IRS unit as x, and the size of the transmitter is 10 cm. Without loss of generality, suppose parameters is b $= 1.5$ m, c $= 2.5$ m and d $= 1$ m, the stretching factor of triangle ABC and triangle ADE is $2/5$. In this circumstance, the minimum area is 4 cm $\times$ 4 cm, which enables the light emitted from the imaging LED entirely propagates through the unit.

Secondly, the influence of IRS height on the NLoS channel gain is of great significance to be investigated. Based on the Lambertian model, the received optical energy equals 0 when the incidence angle is larger than the FoV [28], resulting in the threshold height as

$$\frac{x_{\min}}{\sqrt{d^2 + x_{\min}^2}} = \cos\Phi, \tag{54}$$

which can be calculated as $x_{\min} = d/\tan\Phi$. On the other hand, the channel gain $h^{(2)}_{k,n,l} = 0$ when $x_{\max} = c$, since the cosine of the irradiance angle is 0. Within the interval of $(x_{\min}, x_{\max})$, the gain $h^{(2)}_{k,n,l}$ is real-valued and nonnegative, and therefore there has an optimal x^* to maximize $h^{(2)}_{k,n,l}$ according to the continuity of (5). Nevertheless, it is intractable to search for the closed-form expression of x^*, and numerical results are provided in Fig. 9 to show the NLoS channel gain versus the IRS height x. Specifically, it can be observed that $h^{(2)}_{k,n,l}$ is larger when x is in the middle of the room height. The results also indicate that x^* decreases when the Lambertian index grows from 1 to 5, which is reasonable since the half-intensity radiation angle gets smaller.

To explore the effect of room size, the SINR performance versus locations of a single user, which is simultaneously served by four transmitters, is evaluated. Specifically, Fig. 10 denotes the individual SINR with the room size of 8 m $\times$ 8 m $\times$ 3 m, and Fig. 11 represents the result when the room size is 12 m $\times$ 12 m $\times$ 3 m while other conditions remain unchanged. In the latter case, the locations

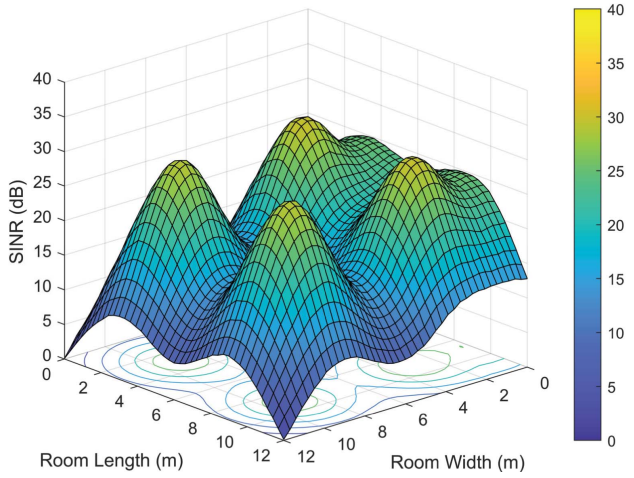

Fig. 11. SINR performance when the room size is 12 m × 12 m × 3 m, and an IRS is deployed on one wall.

of LEDs are at (3 m, 3 m, 3 m), (3 m, 9 m, 3 m), (9 m, 3 m, 3 m), and (9 m, 9 m, 3 m), and IRS units are evenly in the rectangle with (0 m, 1 m, 1.5 m) and (0 m, 11 m, 2.5 m) as corners. As shown in the results, the locations that are close to four LEDs have a higher SINR than other places, and the SINR decreases globally with the increase of the room size. Then, the place close to the wall with IRS achieves higher SINR performance compared to other room edges, and such an improvement is negligible when the user is far away from the IRS. To sum up, the numerical results here reveal that the influence of IRS on VLC systems weakens in large rooms, and therefore, IRS-aided VLC is more suitable to enhance short range communications.

V. Conclusion

In this paper, both LoS and NLoS channel gains in IRS-aided VLC systems are discussed under the point source assumption, and the overall SE maximization process is formulated into a combinatorial optimization problem. Then, an alternating optimization algorithm is proposed to iteratively optimize the resource management, where the frozen variable algorithm deals with the IRS configuration, and the MM algorithm is utilized for user association and power allocation. Though the global optimal point is intractable to obtain for such an NP-hard problem, the proposed algorithm offers a complexity acceptable way to search for a suboptimal result, and the computational complexity is even less when the condition $K < L$ holds. Numerical results demonstrate that the proposed power allocation and IRS configuration policies perform superior to other baselines, and the overall SE increases almost linear to the numbers of IRS units and reflection factor. Furthermore, high path loss of the optical channel gain limits the affected area of VLC IRS, which requires multiple IRSs to facilitate communications in reality. Benefiting from the reconfigurability and passivity, IRS can dramatically improve the SE performance of VLC and ease the blockage problems in optical wireless communications, and therefore the technology of IRS-aided VLC shows great potential in enhancing future wireless communication capabilities.

Appendix A
Non-Concavity of SE With Respect to P and F

To justify the non-concavity of SE function with respect to the power allocation matrix $\mathbf{P}$, a two-dimensional case is considered and the expressions of individual SINR can be expressed as

$$\gamma_1 = \frac{a_1^2 p_1^2}{\sigma_1^2 + a_2^2 p_2^2}, \quad \gamma_2 = \frac{b_2^2 p_2^2}{\sigma_2^2 + b_1^2 p_1^2}, \tag{55}$$

where a_1, a_2, b_1, b_2, σ_1 and σ_2 are the given parameters and p_1, p_2 are the emission power on two LEDs. Then, the overall SE can be formulated by $R = [\log_2(1 + w\gamma_1) + \log_2(1 + w\gamma_2)]/2$ based on (15), and two functions $f_1(x)$ and $f_2(x)$ are defined for the sake of convenience as

$$f_1(x) = \log_2\left(1 + x^2\right), \; f_2(x; a) = \log_2\left(1 + \frac{1}{x^2 + a^2}\right), \tag{56}$$

where $a \in \mathbb{R}_+$ is a parameter, and the second derivatives are given by

$$\frac{\partial^2 f_1(x)}{\partial x^2} = \frac{2}{\ln 2} \frac{1 - x^2}{(1 + x^2)^2}, \tag{57}$$

$$\frac{\partial^2 f_2(x)}{\partial x^2} = \frac{2}{\ln 2} \frac{3x^4 + (1 + 2a^2)x^2 - a^2(a^2 + 1)}{(x^2 + a^2)^2 (x^2 + a^2 + 1)^2}. \tag{58}$$

Particularly, when p_2 is fixed as a constant, the overall SE can be rewritten as

$$R(p_1|\, p_2) = \frac{1}{2}\left\{ f_1\left(p_1 \sqrt{\frac{w a_1^2}{\sigma_1^2 + a_2^2 p_2^2}}\right) + f_2\left(p_1 \sqrt{\frac{b_1^2}{w b_2^2 p_2^2}}\right)\right\}, \tag{59}$$

where $a = \sigma_2 / \sqrt{w b_2^2 p_2^2}$. Afterwards, its second derivative is calculated as

$$\frac{\partial^2 R(p_1|\, p_2)}{\partial p_1^2} = \frac{w a_1^2}{2(\sigma_1^2 + a_2^2 p_2^2)} \frac{\partial^2 f_1(x)}{\partial x^2}\Big|_{x = p_1 \sqrt{\frac{w a_1^2}{\sigma_1^2 + a_2^2 p_2^2}}} + \frac{b_1^2}{2 w b_2^2 p_2^2} \frac{\partial^2 f_2(x)}{\partial x^2}\Big|_{x = p_1 \sqrt{\frac{b_1^2}{w b_2^2 p_2^2}}}. \tag{60}$$

When the parameters are given by $a_1 = a_2 = b_1 = b_2 = \sigma_1 = \sigma_2 = 1$, two cases with $P_1 = 6$, $P_2 = 3$ and $P_1 = 5$, $P_2 = 2$ lead to positive and negative second derivatives, respectively, which indicates that the function $R(p_1|p_2)$ has uncertain concave-convex property. Therefore, the overall SE function is a noncancave function with respect to variable $\mathbf{P}$ since its projection function on p_1 is nonconcave.

As for the concave/convex properties of $R(\mathbf{F})$ under the relaxed constraint $0 \le f_{l,k} \le 1$, we also consider a special case with $L = K = 2$. By setting $f_{1,2} = 0$ and fixing $f_{2,1}$ and $f_{2,2}$ as constants, the expressions of SINR $\gamma_1(f_{1,1})$ and $\gamma_2(f_{1,1})$ are structurally the same as (55), resulting in the non-concavity of $R(\mathbf{F})$ according to the derivation in the previous discussions.

APPENDIX B
PROOF ON THE CONCAVITY OF TWO APPROXIMATE FUNCTIONS

1) The Function $f_k^{(1)}(\boldsymbol{P};\boldsymbol{P}^{(t)})$

Consider the downlink communications of an IRS-aided VLC system, where two users are served by two LEDs and an IRS is deployed on the wall. To optimize the power allocation behavior, an approximate function is given by

$$f_1^{(1)}(\mathbf{P};\mathbf{P}^{(t)}) = 2\eta\left(x_1^*\right)\log_2\left(p_1\right) - \eta\left(x_1^*\right)\log_2\left(\sigma_1^2 + a_2^2 p_2^2\right) + \eta\left(x_1^*\right)\log_2\left(wa_1^2\right) + \xi\left(x_1^*\right), \tag{61}$$

where the Hessian matrix can be calculated as

$$\left[\frac{\partial^2 f_1^{(1)}(\mathbf{P};\mathbf{P}^{(t)})}{\partial P_1 \partial P_2}\right] = -\frac{2\eta(x_1^*)}{\ln 2}\begin{pmatrix} \dfrac{1}{p_1^2} & 0 \\ 0 & \dfrac{a_2^2(\sigma_1^2 - a_2^2 p_2)}{(\sigma_1^2 + a_2^2 p_2^2)^2} \end{pmatrix}, \tag{62}$$

which is an indefinite matrix depending on the relation between σ_1^2 and $a_2^2 p_2$. Therefore, since the concavity is no longer maintained for the projection function, $f_1^{(1)}(\mathbf{P};\mathbf{P}^{(t)})$ is not a concave function neither.

2) The Function $f_k^{(2)}(\boldsymbol{P};\boldsymbol{P}^{(t)})$

In general, the function $f_k^{(2)}(\mathbf{P};\mathbf{P}^{(t)})$ is formulated based on (44). We define $\mathbf{H}_{\mathcal{P}}^{(k)} = [\mathcal{P}_{(l_1,l_2)}^{(k)}]_{L\times L}$ is the Hessian matrix, and each element $\mathcal{P}_{(l_1,l_2)}^{(k)}$ is the second partial derivative as

$$\mathcal{P}_{(l_1,l_2)}^{(k)} = -\frac{\left(\mathbf{h}_{k,l_1}^{(2)T}\mathbf{g}_{l_1} + h_{k,l_1}^{(1)}\right)\left(\mathbf{h}_{k,l_2}^{(2)T}\mathbf{g}_{l_2} + h_{k,l_2}^{(1)}\right) f_{l_1,k} f_{l_2,k}}{\ln 2\left\{\left[\mathbf{H}_k^{(2)}\mathrm{vec}(\mathbf{G}) + \mathbf{h}_k^{(1)}\right]^T \mathbf{P}\mathbf{f}_k\right\}^2 / \left(2\eta\left(x_1^*\right)\right)} - \frac{2\rho_k^2\eta(x_1^*)}{x_2^*\ln 2}\sum_{i=1,i\neq k}^{K} f_{l_1,i} f_{l_2,i} h_{i,l_1}^{(1)} h_{i,l_2}^{(1)}. \tag{63}$$

Then, the Hessian matrix can be further rewritten as

$$\mathbf{H}_{\mathcal{P}}^{(k)} = \frac{-\left(2\eta\left(x_1^*\right)/\ln 2\right)\mathbf{b}\mathbf{b}^T}{\left\{\left[\mathbf{H}_k^{(2)}\mathrm{vec}(\mathbf{G}) + \mathbf{h}_k^{(1)}\right]^T \mathbf{P}\mathbf{f}_k\right\}^2} - \frac{2\rho_k^2\eta\left(x_1^*\right)}{x_2^*\ln 2}\sum_{i=1,i\neq k}^{K}\mathbf{c}_i\mathbf{c}_i^T, \tag{64}$$

where $\mathbf{b} \in \mathbb{R}_+^{L\times 1}$ and $\mathbf{c} \in \mathbb{R}_+^{L\times 1}$ are vectors as

$$\mathbf{b} = \left[\mathbf{H}_k^{(2)}\mathrm{vec}(\mathbf{G})\right] \odot \mathbf{f}_k + \mathbf{h}_k^{(1)} \odot \mathbf{f}_k, \quad \mathbf{c}_i = \mathbf{h}_i^{(1)} \odot \mathbf{f}_i. \tag{65}$$

According to (64), the following inequality ensures for any $\mathbf{x} \in \mathbb{R}_+^{L\times 1}$ that

$$\mathbf{x}^T\mathbf{H}_{\mathcal{P}}^{(k)}\mathbf{x} \leq 0, \tag{66}$$

which indicates $\mathbf{H}_{\mathcal{P}}^{(k)}$ is a negative semidefinite matrix, and consequently, $f_k^{(2)}(\mathbf{P};\mathbf{P}^{(t)})$ is a concave function. Moreover, the Hessian matrix of $\sum_{k=1}^{K} f_k^{(2)}(\mathbf{P};\mathbf{P}^{(t)})$ can be formulated as $\mathbf{H}_{\mathcal{P}} = \sum_{k=1}^{K}\mathbf{H}_{\mathcal{P}}^{(k)}$, which is also negative semidefinite. Based on (64) and (65), the independent components of $\mathbf{H}_{\mathcal{P}}$ include two forms of vectors: $\mathbf{h}_k^{(1)} \odot \mathbf{f}_k$ and $[\mathbf{H}_k^{(2)}\mathrm{vec}(\mathbf{G})] \odot \mathbf{f}_k$, $\forall k \in \mathcal{K}$. Therefore, matrix $\mathbf{H}_{\mathcal{P}}^{(k)}$ is full-rank when the condition $2K \geq L$ holds, which demonstrates that the objective function in (P2-a) is a strong concave function with the order as

$$m^o = -\lambda_{\max}, \tag{67}$$

where $\lambda_{\max}$ is the largest eigenvalue of $\mathbf{H}_{\mathcal{P}}$.

REFERENCES

[1] H. Burchardt, N. Serafimovski, D. Tsonev, S. Videv, and H. Haas, "VLC: Beyond point-to-point communication," *IEEE Commun. Mag.*, vol. 52, no. 7, pp. 98–105, Jul. 2014.

[2] D. Karunatilaka, F. Zafar, V. Kalavally, and R. Parthiban, "LED based indoor visible light communications: State of the art," *IEEE Commun. Surveys Tuts.*, vol. 17, no. 3, pp. 1649–1678, Aug. 2015.

[3] J. M. Kahn and J. R. Barry, "Wireless infrared communications," *Proc. IEEE*, vol. 85, no. 2, pp. 265–298, Feb. 1997.

[4] B. Mamandipoor, K. Moshksar, and A. K. Khandani, "Capacity-achieving distributions in Gaussian multiple access channel with peak power constraints," *IEEE Trans. Inf. Theory*, vol. 60, no. 10, pp. 6080–6092, Oct. 2014.

[5] A. Elmoslimany and T. M. Duman, "On the discreteness of capacity-achieving distributions for fading and signal-dependent noise channels with amplitude-limited inputs," *IEEE Trans. Inf. Theory*, vol. 64, no. 2, pp. 1163–1177, Feb. 2018.

[6] J.-B. Wang, Q.-S. Hu, J. Wang, M. Chen, and J.-Y. Wang, "Tight bounds on channel capacity for dimmable visible light communications," *J. Lightw. Technol.*, vol. 31, no. 23, pp. 3771–3779, Dec. 1, 2013.

[7] K. Ying, H. Qian, R. J. Baxley, and S. Yao, "Joint optimization of precoder and equalizer in MIMO VLC systems," *IEEE J. Sel. Areas Commun.*, vol. 33, no. 9, pp. 1949–1958, Sep. 2015.

[8] T. Wang, F. Yang, J. Song, and Z. Han, "Dimming techniques of visible light communications for human-centric illumination networks: State-of-the-art, challenges, and trends," *IEEE Wireless Commun.*, vol. 27, no. 4, pp. 88–95, Aug. 2020.

[9] L. Feng, H. Yang, R. Q. Hu, and J. Wang, "MmWave and VLC-based indoor channel models in 5G wireless networks," *IEEE Wireless Commun.*, vol. 25, no. 5, pp. 70–77, Aug. 2018.

[10] Q. Wu and R. Zhang, "Intelligent reflecting surface enhanced wireless network via joint active and passive beamforming," *IEEE Trans. Wireless Commun.*, vol. 18, no. 11, pp. 5394–5409, Nov. 2019.

[11] K. Feng, Q. Wang, X. Li, and C. Wen, "Deep reinforcement learning based intelligent reflecting surface optimization for MISO communication systems," *IEEE Wireless Commun. Lett.*, vol. 9, no. 5, pp. 745–749, May 2020.

[12] Z. Wang, L. Liu, and S. Cui, "Channel estimation for intelligent reflecting surface assisted multiuser communications: Framework, algorithms, and analysis," *IEEE Trans. Wireless Commun.*, vol. 19, no. 10, pp. 6607–6620, Oct. 2020.

[13] M. Najafi, B. Schmauss, and R. Schober, "Intelligent reflecting surfaces for free space optical communication systems," *IEEE Trans. Commun.*, vol. 69, no. 9, pp. 6134–6151, Sep. 2021.

[14] M. Najafi and R. Schober, "Intelligent reflecting surfaces for free space optical communications," in *Proc. IEEE Global Commun. Conf. (GLOBECOM)*, Waikoloa, HI, USA, Dec. 2019, pp. 1–7.

[15] A. M. Abdelhady, A. K. S. Salem, O. Amin, B. Shihada, and M.-S. Alouini, "Visible light communications via intelligent reflecting surfaces: Metasurfaces vs mirror arrays," *IEEE Open J. Commun. Soc.*, vol. 2, pp. 1–20, 2021.

[16] G. K. Shirmanesh, R. Sokhoyan, P. C. Wu, and H. A. Atwater, "Electro-optically tunable multifunctional metasurfaces," *ACS Nano*, vol. 14, no. 6, pp. 6912–6920, Jun. 2020.

[17] Y. Hu *et al.*, "Electrically tunable multifunctional polarization-dependent metasurfaces integrated with liquid crystals in the visible region," *Nano Lett.*, vol. 21, no. 11, pp. 4554–4562, Jun. 2021.

[18] W. Tang *et al.*, "Wireless communications with reconfigurable intelligent surface: Path loss modeling and experimental measurement," *IEEE Trans. Wireless Commun.*, vol. 20, no. 1, pp. 421–439, Jan. 2021.

[19] H. Wang *et al.*, "Performance of wireless optical communication with reconfigurable intelligent surfaces and random obstacles," 2020, *arXiv:2001.05715*.

[20] H. Wang *et al.*, "Performance analysis of multi-branch reconfigurable intelligent surfaces-assisted optical wireless communication system in environment with obstacles," *IEEE Trans. Veh. Technol.*, vol. 70, no. 10, pp. 9986–10001, Oct. 2021.
[21] S. Sun, T. Wang, F. Yang, J. Song, and Z. Han, "Intelligent reflecting surface-aided visible light communications: Potentials and challenges," *IEEE Veh. Technol. Mag.*, early access, Dec. 23, 2021, doi: 10.1109/MVT.2021.3127869.
[22] S. Sun, F. Yang, and J. Song, "Sum rate maximization for intelligent reflecting surface-aided visible light communications," *IEEE Commun. Lett.*, vol. 25, no. 11, pp. 3619–3623, Nov. 2021.
[23] S. Aboagye, T. M. N. Ngatched, O. A. Dobre, and A. R. Ndjiongue, "Intelligent reflecting surface-aided indoor visible light communication systems," *IEEE Commun. Lett.*, vol. 25, no. 12, pp. 3913–3917, Dec. 2021.
[24] L. Qian, X. Chi, L. Zhao, and A. Chaaban, "Secure visible light communications via intelligent reflecting surfaces," in *Proc. IEEE Int. Conf. Commun. (ICC)*, Montreal, QC, Canada, Jun. 2021, pp. 1–6.
[25] B. Lin, X. Tang, Z. Ghassemlooy, C. Lin, and Y. Li, "Experimental demonstration of an indoor VLC positioning system based on OFDMA," *IEEE Photon. J.*, vol. 9, no. 2, pp. 1–9, Apr. 2017.
[26] X. Chen and M. Jiang, "Adaptive statistical Bayesian MMSE channel estimation for visible light communication," *IEEE Trans. Signal Process.*, vol. 65, no. 5, pp. 1287–1299, Mar. 2017.
[27] F. R. Gfeller and U. Bapst, "Wireless in-house data communication via diffuse infrared radiation," *Proc. IEEE*, vol. 67, no. 11, pp. 1474–1486, Nov. 1979.
[28] M. Obeed, A. M. Salhab, M.-S. Alouini, and S. A. Zummo, "On optimizing VLC networks for downlink multi-user transmission: A survey," *IEEE Commun. Surveys Tuts.*, vol. 21, no. 3, pp. 2947–2976, 3rd Quart., 2019.
[29] T. Komine and M. Nakagawa, "Fundamental analysis for visible-light communication system using LED lights," *IEEE Trans. Consum. Electron.*, vol. 50, no. 1, pp. 100–107, Feb. 2004.
[30] Q. Wu and R. Zhang, "Towards smart and reconfigurable environment: Intelligent reflecting surface aided wireless network," *IEEE Commun. Mag.*, vol. 58, no. 1, pp. 106–112, Jan. 2020.
[31] M. Bohge, J. Gross, A. Wolisz, and M. Meyer, "Dynamic resource allocation in OFDM systems: An overview of cross-layer optimization principles and techniques," *IEEE Netw.*, vol. 21, no. 1, pp. 53–59, Feb. 2007.
[32] M. Grant, S. Boyd, and Y. Ye. (2009). *CVX: Matlab Software for Disciplined Convex Programming*. [Online]. Available: http://cvxr.com/cvx/
[33] J. Al-Khori, G. Nauryzbayev, M. M. Abdallah, and M. Hamdi, "Joint beamforming design and power minimization for friendly jamming relaying hybrid RF/VLC systems," *IEEE Photon. J.*, vol. 11, no. 2, pp. 1–18, Apr. 2019.
[34] S. Boyd and L. Vandenberghe, *Convex Optimization*. Cambridge, U.K.: Cambridge Univ. Press, 2004.
[35] S. Bubeck, "Convex optimization: Algorithms and complexity," *Found. Trends Mach. Learn.*, vol. 8, nos. 3–4, pp. 231–357, 2015.
[36] D. R. Hunter and K. Lange, "A tutorial on MM algorithms," *Amer. Statist.*, vol. 58, no. 1, pp. 30–37, Feb. 2004.
[37] Y. Sun, P. Babu, and D. P. Palomar, "Majorization-minimization algorithms in signal processing, communications, and machine learning," *IEEE Trans. Signal Process.*, vol. 65, no. 3, pp. 794–816, Feb. 2017.
[38] J. Papandriopoulos, S. Dey, and J. Evans, "Optimal and distributed protocols for cross-layer design of physical and transport layers in MANETs," *IEEE/ACM Trans. Netw.*, vol. 16, no. 6, pp. 1392–1405, Dec. 2008.
[39] A. Wiesel, "Unified framework to regularized covariance estimation in scaled Gaussian models," *IEEE Trans. Signal Process.*, vol. 60, no. 1, pp. 29–38, Jan. 2012.

Shiyuan Sun received the B.S. degree from the Department of Electronic Engineering, Tsinghua University, Beijing, China, in 2020, where he is currently pursuing the Ph.D. degree with the DTV Technology Research and Development Center, Department of Electronic Engineering. His research interests are in the field of visible light communications, wireless communications, and intelligent reflecting surface.

Fang Yang (Senior Member, IEEE) received the B.S.E. and Ph.D. degrees in electronic engineering from Tsinghua University, Beijing, China, in 2005 and 2009, respectively. Currently, he is an Associate Professor with the Department of Electronic Engineering, Tsinghua University. He has published over 180 peer-reviewed journals and conference papers. He holds over 50 Chinese patents and two PCT patents. His research interests are in the fields of power line communication, visible light communication, and digital television terrestrial broadcasting. He is a fellow of IET. He received the IEEE Scott Helt Memorial Award (Best Paper Award in IEEE TRANSACTIONS ON BROADCASTING) in 2015.

Jian Song (Fellow, IEEE) received the B.Eng. and Ph.D. degrees in electrical engineering from Tsinghua University, Beijing, China, in 1990 and 1995, respectively. Currently, he is the Director of the Tsinghua DTV Technology Research and Development Center. He has been working in quite different areas of fiber-optic, satellite and wireless communications, and the power-line communications. He has published more than 300 peer-reviewed journals and conference papers. He holds two U.S. and more than 80 Chinese patents. His current research interest is in the area of digital TV broadcasting. He is a fellow of IET.

Zhu Han (Fellow, IEEE) received the B.S. degree in electronic engineering from Tsinghua University, Beijing, China, in 1997, and the M.S. and Ph.D. degrees in electrical and computer engineering from the University of Maryland, College Park, in 1999 and 2003, respectively. From 2000 to 2002, he was a Research and Development Engineer at JDSU, Germantown, Maryland. From 2003 to 2006, he was a Research Associate with the University of Maryland. From 2006 to 2008, he was an Assistant Professor with Boise State University, Idaho. Currently, he is a John and Rebecca Moores Professor with the Electrical and Computer Engineering Department and the Computer Science Department, University of Houston, Texas. His research interests include wireless resource allocation and management, wireless communications and networking, game theory, big data analysis, security, and smart grid. He received the NSF Career Award in 2010, the Fred W. Ellersick Prize of the IEEE Communication Society in 2011, the EURASIP Best Paper Award for the *Journal on Advances in Signal Processing* in 2015, the IEEE Leonard G. Abraham Prize in the field of Communications Systems (Best Paper Award in IEEE JOURNAL ON SELECTED AREAS IN COMMUNICATIONS) in 2016, and several best paper awards in IEEE conferences. He was an IEEE Communications Society Distinguished Lecturer from 2015 to 2018. He has been an ACM Distinguished Member since 2019 and an AAAS Fellow since 2019. He has been a 1% highly cited researcher since 2017 according to Web of Science. He is also the Winner of the 2021 IEEE Kiyo Tomiyasu Award, for outstanding early to mid-career contributions to technologies holding the promise of innovative applications, with the following citation: "for contributions to game theory and distributed management of autonomous communication networks."